Since January 2020 Elsevier has created a COVID-19 resource centre with free information in English and Mandarin on the novel coronavirus COVID-19. The COVID-19 resource centre is hosted on Elsevier Connect, the company's public news and information website.

Research Article

Binding Adaptation of GS-441524 Diversifies Macro Domains and Down-regulates SARS-CoV-2 de-MARylation Capacity

Aikaterini C. Tsika [1], Angelo Gallo [1], Nikolaos K. Fourkiotis [1], Aikaterini I. Argyriou [1], Sridhar Sreeramulu [2], Frank Löhr [3], Vladimir V. Rogov [4,5], Christian Richter [2], Verena Linhard [2], Santosh L. Gande [2], Nadide Altincekic [2], Robin Krishnathas [2], Isam Elamri [2], Harald Schwalbe [2*], Jan Wollenhaupt [6], Manfred S. Weiss [6] and Georgios A. Spyroulias [1*]

*1 - **Department of Pharmacy,** University of Patras, GR-26504 Patras, Greece*
*2 - **Institute for Organic Chemistry and Chemical Biology,** Center for Biomolecular Magnetic Resonance, Johann Wolfgang Goethe-University Frankfurt, Max-von-Laue-Str. 7, 60438 Frankfurt am Main, Germany*
*3 - **Institute for Biophysical Chemistry,** Center for Biomolecular Magnetic Resonance, Johann Wolfgang Goethe-University Frankfurt, Max-von-Laue-Str. 9, 60438 Frankfurt am Main, Germany*
*4 - **Structural Genomics Consortium (SGC),** Buchmann Institute for Molecular Life Sciences, Max-von-Laue-Str. 15, 60438 Frankfurt am Main, Germany*
*5 - **Institute of Pharmaceutical Chemistry,** Johann Wolfgang Goethe University Frankfurt, Max-von-Laue-Str. 9, 60438 Frankfurt am Main, Germany*
*6 - **Macromolecular Crystallography,** Helmholtz-Zentrum Berlin, Albert-Einstein-Straße 15, D-12489 Berlin, Germany*

***Correspondence to Harald Schwalbe and Georgios A. Spyroulias:** schwalbe@nmr.uni-frankfurt.de (H. Schwalbe), G.A.Spyroulias@upatras.gr (G.A. Spyroulias) @katerina_tsika (A.C. Tsika), @AngeloGallo83 (A. Gallo), @HaraldSchwalbe (H. Schwalbe), @Jan_Wollenhaupt (J. Wollenhaupt), @ManfredSWeiss (M.S. Weiss)*
https://doi.org/10.1016/j.jmb.2022.167720
Edited by C. Kalodimos

Abstract

Viral infection in cells triggers a cascade of molecular defense mechanisms to maintain host-cell homoeostasis. One of these mechanisms is ADP-ribosylation, a fundamental post-translational modification (PTM) characterized by the addition of ADP-ribose (ADPr) on substrates. Poly(ADP-ribose) polymerases (PARPs) are implicated in this process and they perform ADP-ribosylation on host and pathogen proteins. Some viral families contain structural motifs that can reverse this PTM. These motifs known as macro domains (MDs) are evolutionarily conserved protein domains found in all kingdoms of life. They are divided in different classes with the viral belonging to Macro-D-type class because of their properties to recognize and revert the ADP-ribosylation. Viral MDs are potential pharmaceutical targets, capable to counteract host immune response. Sequence and structural homology between viral and human MDs are an impediment for the development of new active compounds against their function. Remdesivir, is a drug administrated in viral infections inhibiting viral replication through RNA-dependent RNA polymerase (RdRp). Herein, GS-441524, the active metabolite of the remdesivir, is tested as a hydrolase inhibitor for several viral MDs and for its binding to human homologs found in PARPs. This study presents biochemical and biophysical studies, which indicate that GS-441524 selectively modifies SARS-CoV-2 MD de-MARylation activity, while it does not interact with hPARP14 MD2 and hPARP15

MD2. The structural investigation of MD•GS-441524 complexes, using solution NMR and X-ray crystallography, discloses the impact of certain amino acids in ADPr binding cavity suggesting that F360 and its adjacent residues tune the selective binding of the inhibitor to SARS-CoV-2 MD.

Introduction

ADP-ribosylation is a reversible fundamental post-translational modification (PTM) implicated in different cellular functions including DNA repair, chromatin remodeling and metabolism. Cellular signaling relies on ADP-ribosylation. It has been linked to human diseases, especially neurological disorders, cancer and inflammation.[1–2] Although it was first identified in 1960s, many aspects regarding the mechanism of this PTM as well as the cellular response and its cascades are yet to be fully investigated.[3] Recently, new interesting findings link this modification to other PTMs such as ubiquitination, SUMOylation and phosphorylation.[4–7] ADP-ribosylation is described as the covalent attachment of a single or multiple ADP-ribose (ADPr) moieties to a protein, a nucleic acid, an antibiotic, or an acetyl group.[8–10] All of the above highlight the paramount impact of this biochemical pathway, which is emerging as a research field of high pharmacological interest.[1–2]

The central molecule in ADP-ribosylation is NAD^+. The term mono-ADP-ribosylation or MARylation is used to describe the transfer of a single unit (single ADPr molecule), while the synthesis and the covalent attachment of linear or branched ADPr chains containing multiple units, it is referred as poly-ADP-ribosylation or PARylation. A specific class of enzymes, ADP-ribosyl transferases (ARTs)[11] convert NAD^+ to ADPr and nicotinamide (NAM). Moreover, ARTs transfer the ADPr molecule to the substrates and thus, are described as "writers" of the ADP-ribosylation process. They are classified into two subgroups: the cholera toxin-like ADP-ribosyl transferases (ARTCs) and the diphtheria toxin-like ADP-ribosyl transferases (ARTDs).[12] In humans 22 ARTs genes have been identified to express 21 ARTs. Four of them correspond to the ARTCs, while 17 are coding the ARTDs, also called poly (ADP-ribose) polymerases (PARPs). These two enzyme subgroups mainly differ in the composition of the amino acids spanning the catalytic core.[13]

ADP-ribosylation is a reversible modification and enzymes that de-ADP-ribosylate substrates are called "erasers"[8]. They are classified into two categories: the ADP-ribosyl-acceptor hydrolases (ARHs) and the macro domain (MD)-containing enzymes; both exhibiting substrate cleavage specificity. Poly(ADP-ribosyl)glycohydrolase (PARG), a member of the second group, hydrolyze ADPr chains efficiently but differs from the other members in the group due to its inability to remove the terminal ADPr unit. In humans, there are 12 proteins that contain MD and only 4 of them up to date are known for possessing the ability to hydrolyze ADPr groups.[1]

This divergence of this enzymatic property between the members of the human proteins containing MD can be found in all kingdoms of life. Indeed, MDs are conserved structural motifs consisting of 130–190 amino acids. They exhibit a characteristic $\alpha/\beta/\alpha$ sandwich fold and can be found in unicellular or multicellular, prokaryotic or eukaryotic organisms and viruses. Despite their structural similarity they differ in many functional aspects[14]. In the ADP-ribosylation modification, MDs can act as "readers", recognizing PARylated or MARylated substrates, or/and as "erasers" hydrolyzing the covalent attached ADPr moieties. MDs are also key elements of the viral replication machinery[15] and they are also implicated in DNA damage repair[2] having nucleic acid binding capacity. The different binding affinity towards free ADPr or the covalently bound ADPr is one of the key factors to fully understand their function[14,16–17]. It is still unknown how the specificity of MARylated or PARylated sites is influenced by their surroundings and whether or/and how plasticity[18–19] of the loops that connect the structural elements of MDs contribute to their functional properties.

ADP-ribosylation is also implicated in inflammation and in immune response. In fact, several PARPs are involved in this response. Amongst the members of the human PARP family, *parp9*, *parp12*, *parp13*, and *parp14* genes, expression is stimulated by interferon IFN while PARP7, PARP10 and PARP15 inhibit viral replication.[20–22] Notably, PARP9, PARP14 and PARP15 are also the three human PARPs containing tandem MDs[16], whose functional role of each one or all as a whole has not been elucidated yet. Furthermore, it has been reported that PARP9 and PARP14 cross-regulate macrophage activation[23] and the corresponding genes are evolved under positive selection[24] suggesting an adaptation of the host to face pathogens.[24]

Characteristic type of pathogens that contain MDs are ss(+)RNA viruses.[25–27] There are four virus families in which MDs have been found, namely *Togaviridae, Coronaviridae*, *Matonaviridae* and *Hepeviridae*[16]. Up to date, many X-rays and NMR structures have been deposited to the Protein Data Bank (PDB) revealing the structural characteristics of MDs fall into the first two families[18,28–31]. In

general, these MDs belong to MacroD-type class, and they retain most of the general functions including the de-MARylation activity[14,32–33]. In recent years, the role of viral MDs has increasingly been considered as a mechanism that pathogens use to counteract the antiviral host response, especially the mechanisms exerted by PARPs.[15,34–35]

PARP12 and PARP14 seem to play a role in the pathogenicity of viruses and lately it was proved the ability of SARS-CoV-2 MD to hydrolyze PARP14 and PARP9/DTX3L mediated ADP-ribosylation of substrates.[36–37] SARS-CoV-2, which belongs to *Coronaviridae,* is the pathogen responsible for the COVID-19 pandemic and the first known case was reported in China, in December 2019. Its MD is located at the N-terminal region of its non-structural Protein 3 (nsP3), which is the largest (200 kDa) multi domain nsP encoded by ORF1ab in the SARS-CoV-2 genome[38]. According to many studies, viral MDs are crucial for virus replication and pathogenicity[15,39–40]. Furthermore, viruses harboring inactive MD mutants are sensitized to the antiviral effect of interferon IFN, revealing its significance in countering the IFN-stimulated genes (ISGs) activity.[41]

Recently, the COVID19-NMR consortium has established protocols for the production and purification of 23 of the 30 SARS-CoV-2 proteins with the aim of aiding downstream biomedical application.[42] In this context viral MDs can be potential therapeutic targets especially if the issue of specificity between viral and human MDs is resolved, and therefore eliminating potential adverse effects. Shedding light on the differences in the ligand binding and catalytic pocket between human and viral MDs, will allow to unravel the functional differences among MDs to design, new, promising scaffolds, in the quest of compounds with enhanced selectivity and binding properties towards viral MDs.

Remdesivir (GS-5734) is one of the antiviral drugs administrated to treat COVID-19.[43–44] Remdesivir is an adenosine nucleotide analogue that targets SARS-CoV-2 RNA-dependent RNA polymerase (RdRp). Intracellularly it is enzymatically converted to an active metabolite, GS-441524, which has been reported to exhibit better plasma stability.[45–47] The phosphorylated form of GS-441524 inhibits the RdRp viral genome replication.[48] Recent studies report the effective inhibition of viral replication through direct administration of GS-441524 in mouse models.[49] Crystal structure studies show that the GS-441524 being a nucleotide analogue binds to the ADPr binding pocket of SARS-CoV-2 MD.[50]

In 2018, a study revealed that GS-441524 acts effectively against feline infectious peritonitis virus (FIPV) that causes peritonitis in cats. FIPV belongs to *Alphacoronaviruses* 1 and contain a MD, although its role in the viral infection has not been reported.[51]

In this study, we report the modulation of the SARS-CoV-2 MD function upon GS-441524 binding, providing experimental evidence for the inhibition of MD's de-MARylation activity. Additionally, the comparative study with other viral MDs from *Coronaviruses* (CoVs) and *Alphaviruses* as well as two closely related human counterparts reveals striking differences amongst them. Implementation of high-resolution NMR along with other biophysical studies and biochemical assays, deciphers the structural basis of the MD ligand binding capacity and the variable inhibition effect of GS-441524 to the viral MDs, as probed by western blot (WB) analysis of the de-MARylation activity. Since MDs emerge as new, druggable viral protein targets, these results, provide valuable hints on the design of new organic skeletons, properly functionalized, to discriminate the MDs targets, not only among human counterparts, but also among viral members.

Results and Discussion

De-MARylation of hPARP10 CD by CoVs and Alphaviruses MDs is regulated by excess of ADPr and GS-441524

Based on the reported de-MARylation activity of viral MDs[52], we designed and performed an assay to examine their activity in the presence of potential low molecular weight inhibitors. The assay has initially been utilized to test the effect of ADPr as a "competitive" inhibitor of enzymatic activity.[33,53] We thus used ADPr, the physiological ligand, as a positive control due to its high affinity and tested remdesivir and its' metabolite, GS-441524, for their potential activity towards viral MDs as close analogs of adenosine. Because the catalytic domain of human PARP10 (hPARP10 CD) can be auto-MARylated, it is widely used as probe for studying the de-MARylation activity of viral MDs.[33] Incubation of hPARP10 CD with CoVs and *Alphaviruses* MDs at equal molar ratio (hPARP10 CD:MD equal to 1:1) was conducted at 30 °C and 250 rpm while samples were taken at 0, 5, 10, 20, 30 and 60 min of the reaction. The reaction was performed in the presence and the absence of each of the ligands (e.g., ADPr, remdesivir, GS-441524 and chlorinated GS-441524 analogue) in 100- and 500-fold excess.

The results of the immunoblotting analysis showed that both ADPr and GS-441524 affect SARS-CoV-2 de-MARylation activity. Bands corresponding to the MARylated hPARP10 CD were detected even at longer time in assays using both compounds (Figure 1(a)). In the case of remdesivir, the rate of signal decay is comparable to the free form (Figure 1(a)).

The time dependence of the de-MARylation assay data has been quantified. The initial substrate decay rate (k) for SARS-CoV-2 MD is

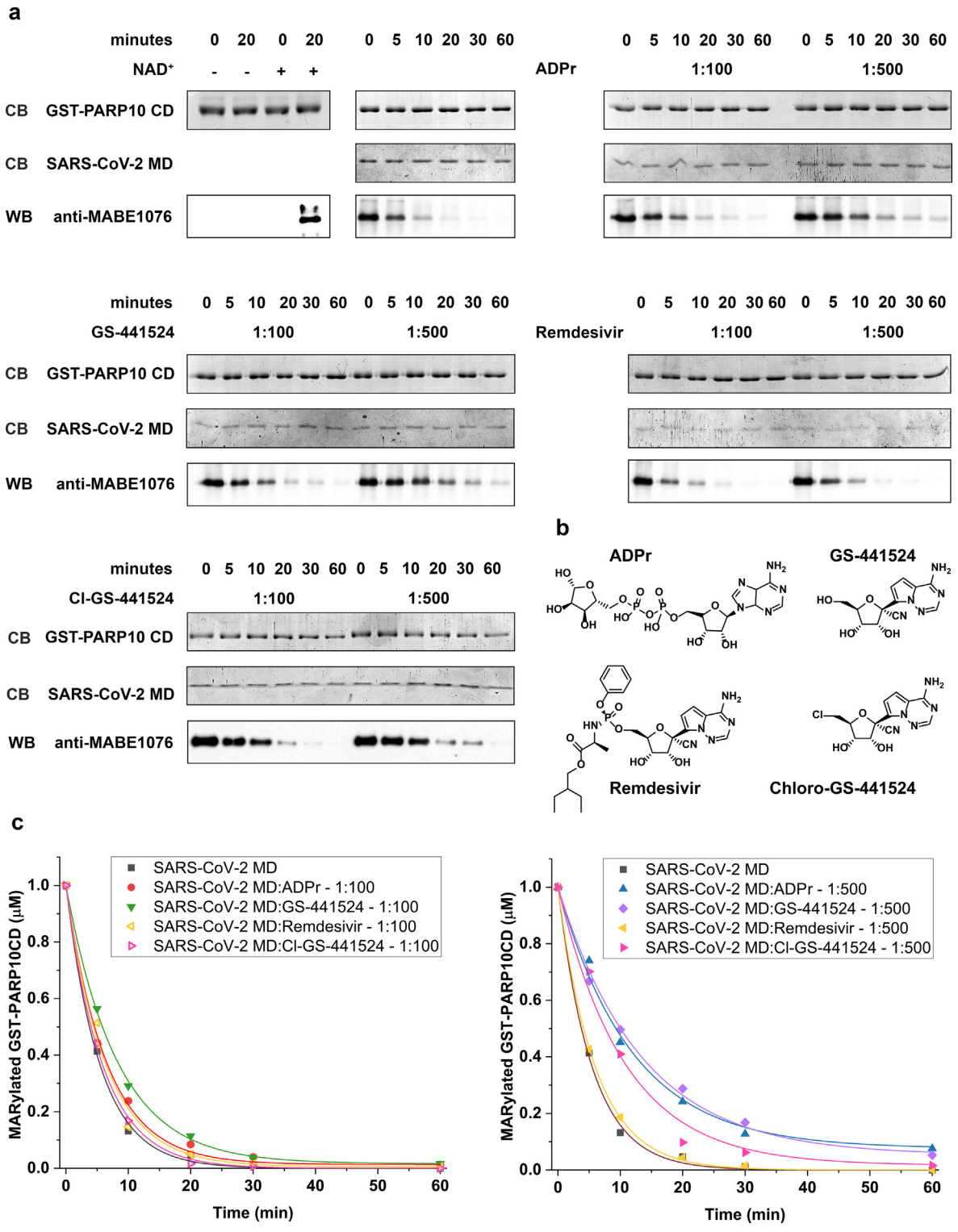

Figure 1. (a) De-MARylation activity of SARS-CoV-2 MD tested by immunoblotting (WB). SARS-CoV-2 MD was incubated with MARylated GST-hPARP10 CD at molar ratio 1:1 in absence and presence of each depicted compound and excess. Samples were obtained at the indicated times. Coomassie Blue (CB) stain was used for the total protein amount verification. These experiments were performed in triplicates. (b) Chemical structures of the used compounds (left to right) ADPr, remdesivir, GS-441524 and its chlorinated analogue. (c) Quantification results for the experiments from panel (a) in 100 (left) and 500 (right) times excess for each of the used compounds. For this procedure the bands from each experiment were quantified by Image Lab software. Plots and rate quantification were obtained by Origin2019b after summarizing the results from each independent experiment for the tested compounds.

Table 1 Initial substrate decay rate k (μM/min) calculated for each of the studied MDs and the respective assay.

	Free	ADPr 1:100	ADPr 1:500	GS-441524 1:100	GS-441524 1:500	Remdesivir 1:100	Remdesivir 1:500	Cl-GS-441524 1:100	Cl-GS-441524 1:500
SARS-CoV-2	0.184 ± 0.006	0.154 ± 0.006	0.084 ± 0.005	0.121 ± 0.002	0.075 ± 0.003	0.157 ± 0.012	0.169 ± 0.002	0.17 ± 0.004	0.093 ± 0.007
SARS-CoV-2^{F360N}	0.237 ± 0.001	0.205 ± 0.010	0.098 ± 0.002	0.210 ± 0.004	0.140 ± 0.005	*	*	*	*
SARS-CoV-2$^{A358V/F360N}$	0.190 ± 0.010	*	0.067 ± 0.005	*	0.127 ± 0.01	*	*	*	*
SARS-CoV-2$^{F360N/D361S}$	0.213 ± 0.006	*	0.081 ± 0.004	*	0.160 ± 0.007	*	*	*	*
SARS-CoV-1	0.244 ± 0.013	0.182 ± 0.005	0.104 ± 0.001	0.198 ± 0.009	0.167 ± 0.008	*	*	*	*
MERS-CoV	0.202 ± 0.009	0.137 ± 0.003	0.061 ± 0.005	0.167 ± 0.012	0.152 ± 0.002	*	*	*	*
MERS-CoV^{N410F}	0.233 ± 0.000	*	0.072 ± 0.009	*	0.163 ± 0.007	*	*	*	*
CHIKV	0.213 ± 0.003	0.119 ± 0.002	0.077 ± 0.005	0.179 ± 0.003	0.162 ± 0.001	*	*	*	*
MAYV	0.207 ± 0.002	0.100 ± 0.005	0.068 ± 0.002	0.190 ± 0.002	0.153 ± 0.003	*	*	*	*
VEEV	0.331 ± 0.005	0.195 ± 0.004	0.108 ± 0.004	0.273 ± 0.002	0.264 ± 0.002	*	*	*	*

*Experiments not conducted.

found 0.184 ± 0.006 μM/min. The presence of ADPr at 500 times excess results in more than two-fold reduced decay rate (k = 0.084 ± 0.005 μM/min) while remdesivir caused only a minor difference compared to the initial rate (k = 0.169 ± 0.002 μM/min). Notably, the same reduction induced by ADPr was also observed for GS-441524 (k = 0.075 ± 0.003 μM/min). The effect of the chlorinated analogue of GS-441524 seems that affects in the same way as the GS-441524 the activity of SARS-CoV-2 MD (k = 0.093 ± 0.007 μM/min) (Figure 1(c), Table 1).

We also compared the inhibition effect of GS-441524 on other viral MDs including MDs from SARS-CoV-1, MERS-CoV, CHIKV, MAYV and VEEV using the same protocol applied for SARS-CoV-2 MD (Figures 2(a), 2(b), 3(a) and 3(b)). The initial substrate decay rates (k) for the free, the ADPr (1:100 and 1:500) and the GS-441524 (1:100 and 1:500) forms reported in Table 1. The values for the free form of the CoVs MDs are found to be comparable to those reported in a recently published study.[52] The ADPr inhibits the de-MARylation activity of all enzymes and reveal similar patterns for all MDs, decreasing the k values close to 55–60%. On the other hand, GS-441524 had smaller impact to all the other viral MDs than in SARS-CoV-2 MD (a 500-fold excess of GS-441524 induces a 60% reduction of the k value for SARS-CoV-2 MD, compared to 15–32% reduction of the other viral MDs).

The results reported herein thus indicate that GS-441524 influence selectively and negatively the *in vitro* de-MARylation ability and consequently slows down the hydrolysis rate of SARS-CoV-2 MD, while this compound has a smaller impact on the other closely related viral MDs.

Mapping the ADPr and GS-441524 binding sites on CoVs and Alphaviruses MDs by NMR-driven titration indicates a different affinity

To further investigate the interaction between MDs, ADPr and GS-441524 at an atomic level, we performed NMR-driven titrations. ADPr and GS-441524 were titrated to the three CoVs MDs and their chemical shift changes were analyzed and then compared to define the binding cleft and the binding affinity of GS-441524 compared to the physiological MD ligand.

All the three CoVs MDs exhibit a similar behavior during the titrations with ADPr while for the *Alphaviruses* the respective studies have been published elsewhere.[18,31] The CSPs analysis clearly shows that upon binding the same protein regions are affected. The chemical shift perturbation analysis reveals that the residues exhibiting meaningful CSPs (value > threshold, see Materials and Methods) belong to the loops connecting the following secondary structure segments: β2-α1, β5-α4,β6-α5,β7-α6 (Figures 4(a), 5(a), 6(a)). These regions are distinctive for these proteins, and they

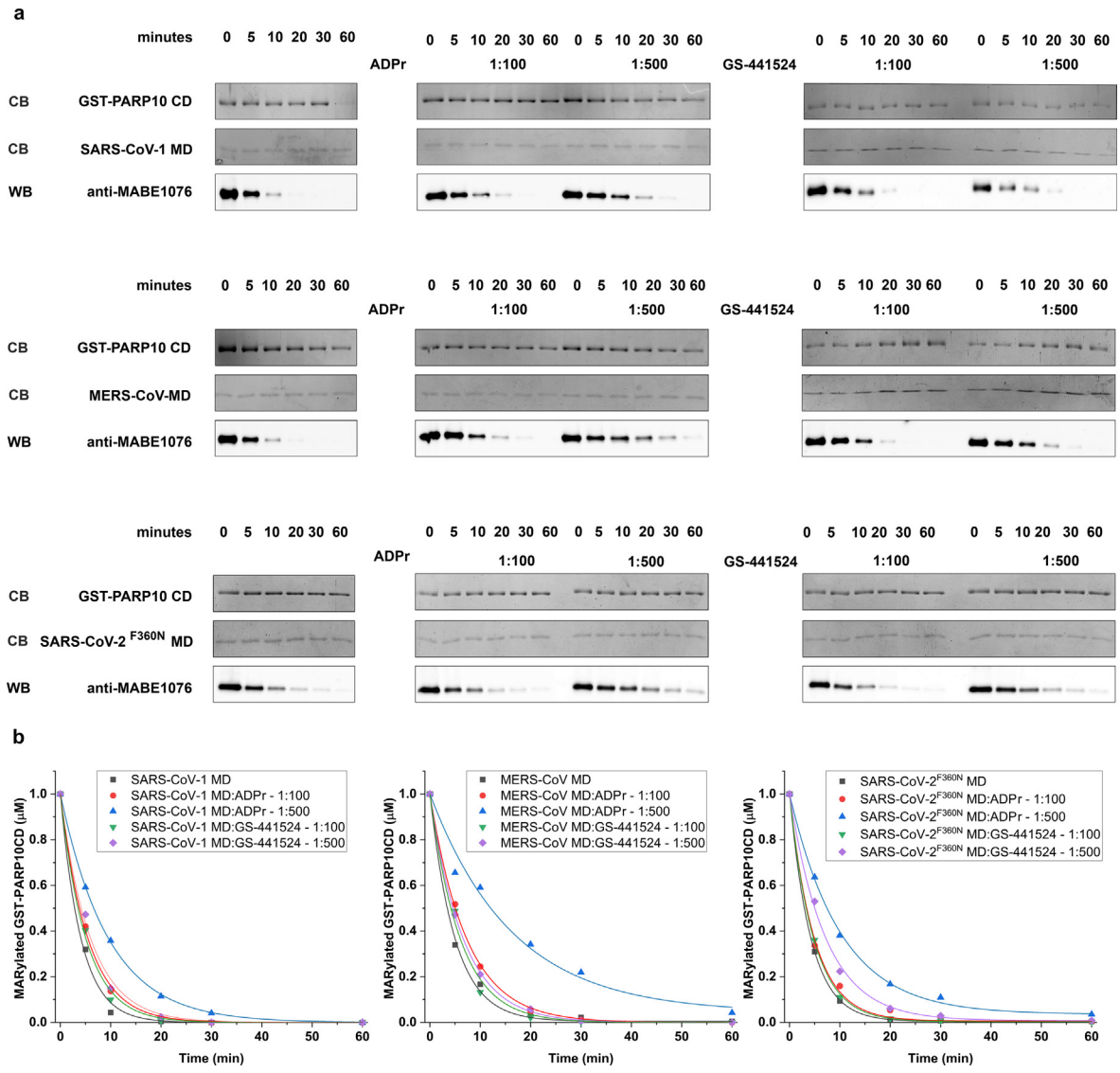

Figure 2. (a) De-MARylation activity of SARS-CoV-1, MERS-CoV and SARS-CoV-2^{F360N} MDs tested by immunoblotting (WB). MDs were incubated with MARylated GST-hPARP10 CD at molar ratio 1:1 in absence and presence of each depicted compound and excess. Samples were obtained at the indicated times. Coomassie Blue (CB) stain was used for the total protein amount verification. These experiments were performed in triplicates. (b) Quantification results for the experiments from panel (a) for SARS-CoV-1 (left), MERS-CoV (middle) and SARS-CoV-2^{F360N} mutant (right) MDs. For this procedure the bands from each experiment were quantified by Image Lab software. Plots and rate quantification were obtained by Origin2019b after summarizing the results from each independent experiment for the tested compounds.

define the ADPr binding cleft as also shown by the reported NMR and crystal structures of these MDs in complex with ADPr (PDB ID: 6YWL, 2FAV, 5DUS).[53,28]

Namely, in SARS-CoV-2 MD•ADPr complex (PDB ID: 6YWL), the side chain of D226 and the backbone of adjacent I227, which are located in the β2-α1 loop, interact with the amino group of the adenine and the N1 atom of the purine ring, respectively. A recently discussed unique feature is the stabilization of the adenine nucleobase by interaction with the aromatic ring of F360 through an edge-to-face interaction and a hydrogen bond of its backbone with the N2 atom of the adenine ring.[36] This interaction is also present and demonstrated by meaningful CSPs for residues mapped on β7-α6 loop. Note that these regions are affected by ADPr binding also in SARS-CoV, MERS-CoV MDs that possess an asparagine residue (N338 and N155 numbering according to PDB IDs: 2ACF and 5HIH) at the F360 position in SARS-CoV-2 MD (Figures 4(a), 5(a), 5(b)). In both complexes, this loop is close to the inhibitor (<5Å), while only for SARS-CoV-1 polar contact has been reported

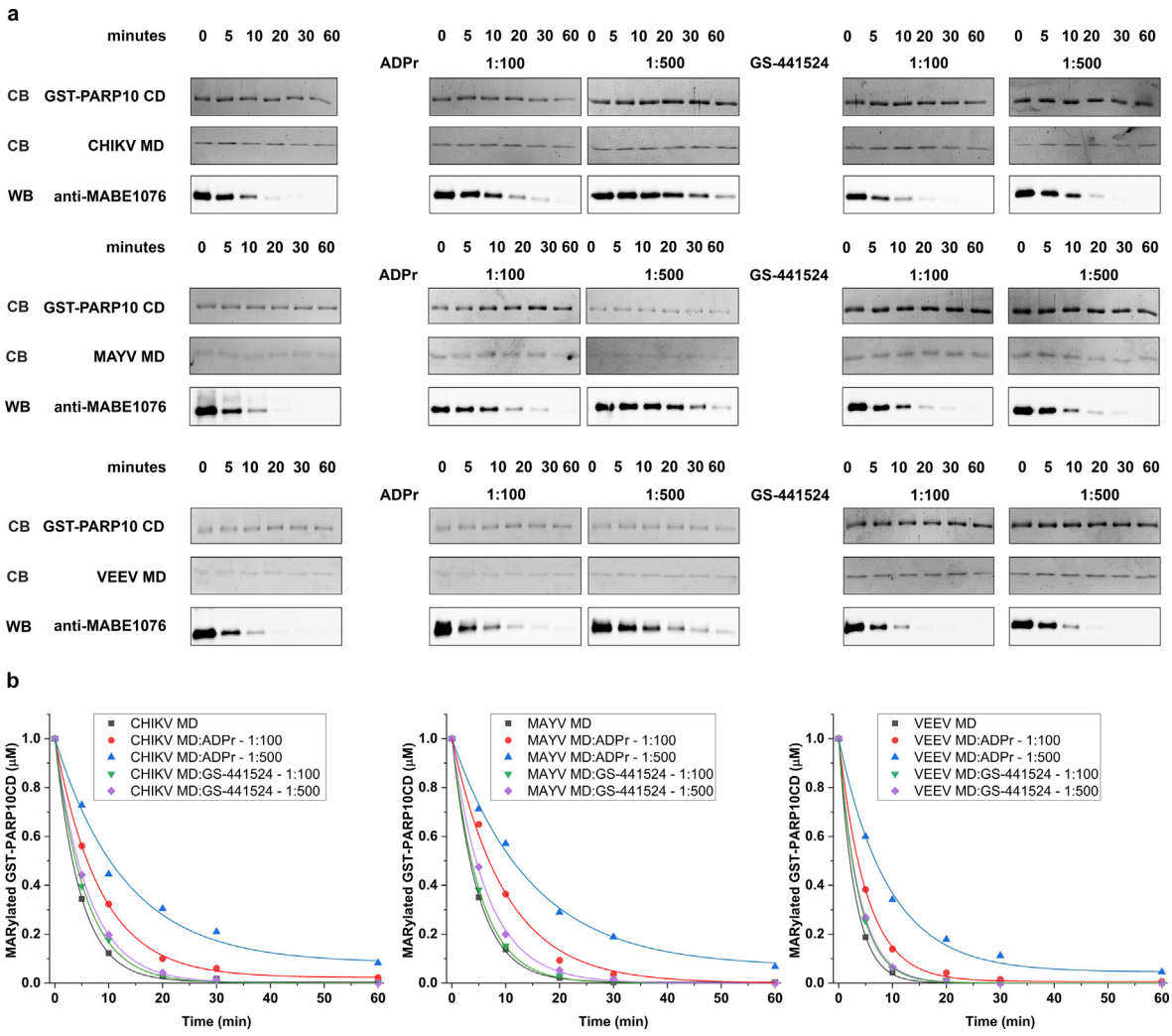

Figure 3. (a) De-MARylation activity of CHIKV, MAYV and VEEV MDs tested by immunoblotting (WB). MDs were incubated with MARylated GST-hPARP10 CD at molar ratio 1:1 in absence and presence of each depicted compound and excess. Samples were obtained at the indicated times. Coomassie Blue (CB) stain was used for the total protein amount verification. These experiments were performed in triplicates. (b) Quantification results for the experiments from panel (a) for CHIKV (left), MAYV (middle) and VEEV (right) MDs. For this procedure the bands from each experiment were quantified by Image Lab software. Plots and rate quantification were obtained by Origin2019b after summarizing the results from each independent experiment for the tested compounds.

between the adenine ring and this amino acid. The residues at this position might also play a role in proximal ribose contacts in other Macro-D-type structures showing also significant reorientation compared to the free protein.[18,54] This phenylalanine is also present in human hPARP15 MD2 as F426. Its crystal structure with ADPr (PDB ID: 3V2B) shows that the phenylalanine ring of F426 establishes a π-π stacking interaction with the adenine ring and the backbone of the neighboring glutamine serves as a hydrogen bond acceptor for the stabilization of one of the OH group of the proximal ribose.

Loop β6-α5 contains one of the most conserved motifs, G- I/V- F/Y, within the Macro-D-type structural family. The two phosphate groups are interacting mainly through the backbone amide groups of these amino acids. The loop β5-α4 shows meaningful CSPs in all studied MDs due to the vicinity with the segment β6-α5 even though there are no direct contacts observed in other structures, so far.

Moreover, the ADPr cleft consists of two highly conserved regions that contribute to ADPr coordination. The β3-α2 loop is essential for the stabilization of the distal ribose, and it involves N241-N244 and the G250-G252 (SARS-CoV-2 numbering). Surprisingly, amino acids spanning loop β3-α2 in SARS-CoV-2 and SARS-CoV-1 MDs could not be identified in the complex forms, whereas the segment A220-H227 (SARS-CoV-1 MD numbering), belonging to this loop, has been

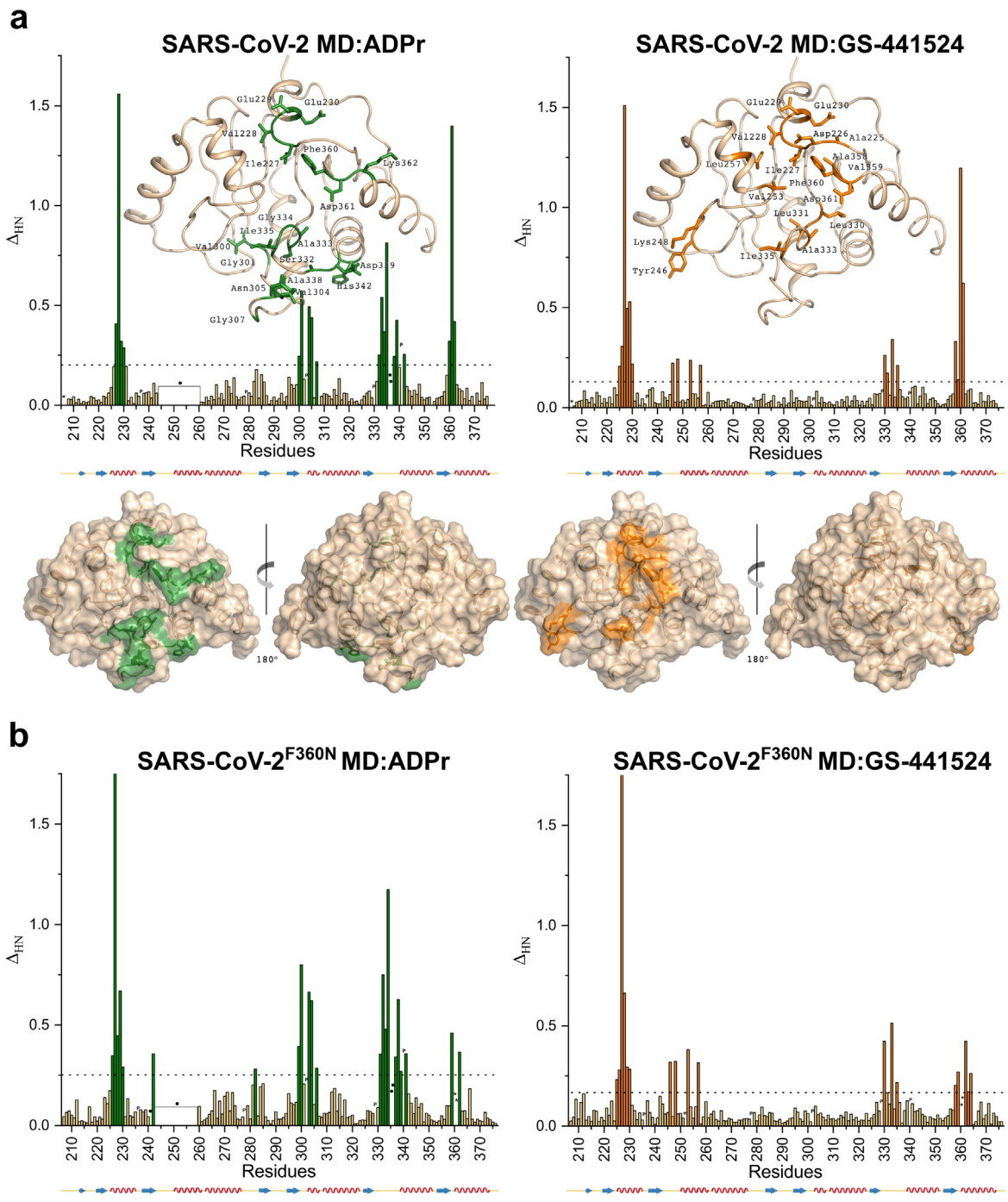

Figure 4. (a) Plots of the combined amide chemical shift changes, $\Delta\delta$, induced by ADPr (left) and GS-441524 (right) binding at versus SARS-CoV-2 MD amino acid sequence at 1:10 molar ratio of protein:ligand. In each plot, the dotted line indicates the applied threshold, an asterisk indicates an unassigned residue of free MD, p indicates a proline residue, and a dot indicates a residue whose HN resonance could not be detected at final titration step. Insets at each plot indicate the mapping of the residues exhibiting meaningful CSPs (value > threshold). Below mapping as in inset on the surface representation of SARS-CoV-2 MD. Mapping has been performed using the PDB ID 6WEY. (b) Plots of combined amide chemical shift changes, $\Delta\delta$, induced by binding ADPr (left) and GS-441524 (right) versus SARS-CoV-2^{F360N} MD mutant amino acid sequence at 1:10 molar ratio of protein:ligand. In each plot, the dotted line indicates the applied threshold, an asterisk indicates an unassigned residue of free MD, p indicates a proline residue, and a dot indicates a residue whose HN resonance could not be detected at final titration step.

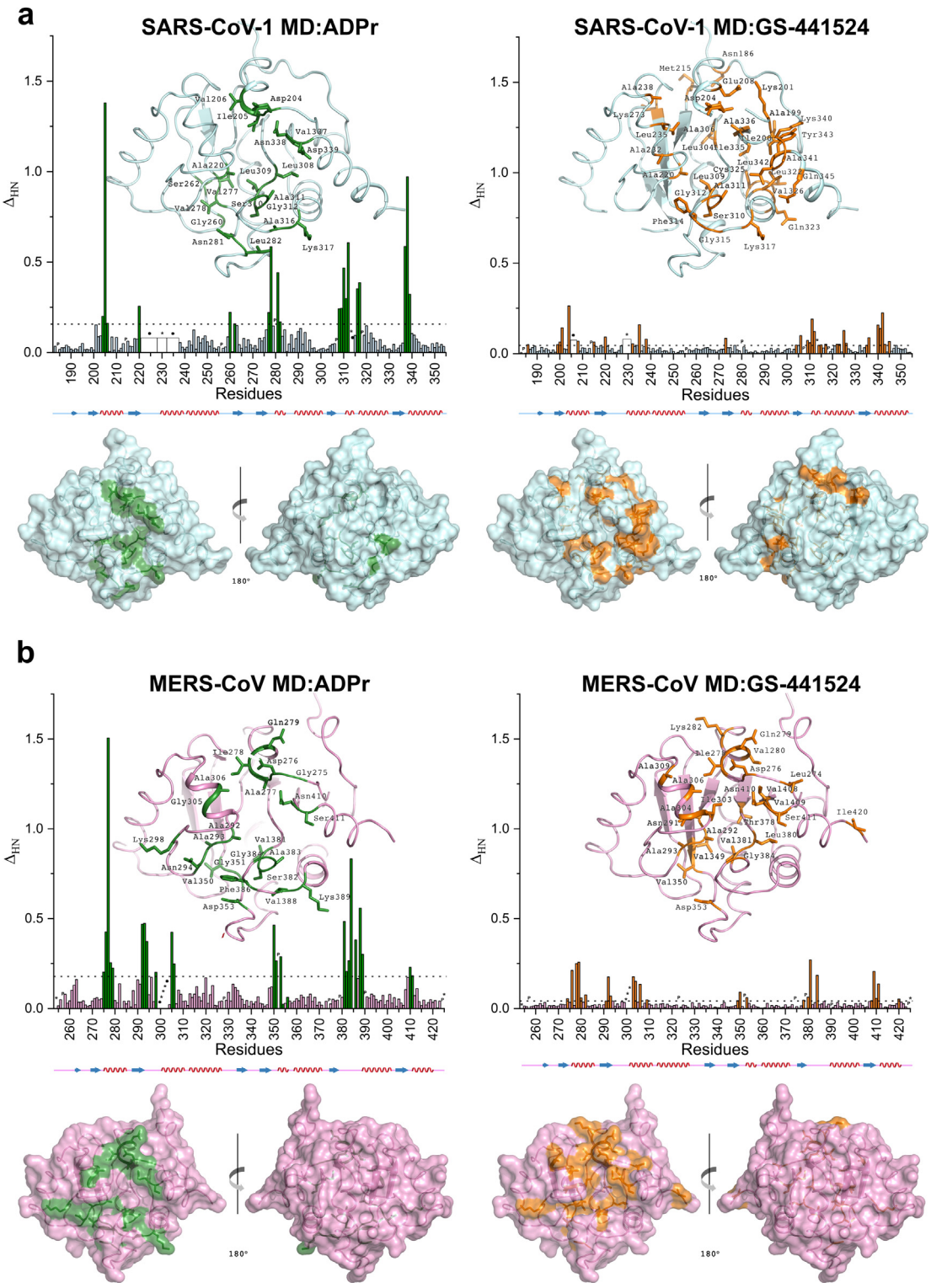

Figure 5. Plots of the combined amide chemical shift changes, $\Delta\delta$, induced by ADPr (left) and GS-441524 (right) binding versus (a) SARS-CoV-1 MD and (b) MERS-CoV MD amino acid sequence at 1:10 molar ratio of protein: ligand. In each plot, the dotted line indicates the applied threshold, an asterisk indicates an unassigned residue of free MD, p indicates a proline residue, and a dot indicates a residue whose HN resonance could not be detected at final titration step. Insets at each plot indicate the mapping of the residues exhibiting meaningful CSPs (value > threshold). Lower panel from each diagram the mapping as in insets on the surface representation. Mapping has been performed on SARS-CoV-1 MD and MESR-CoV MD using the PDB IDs 2ACF and 5HIH respectively.

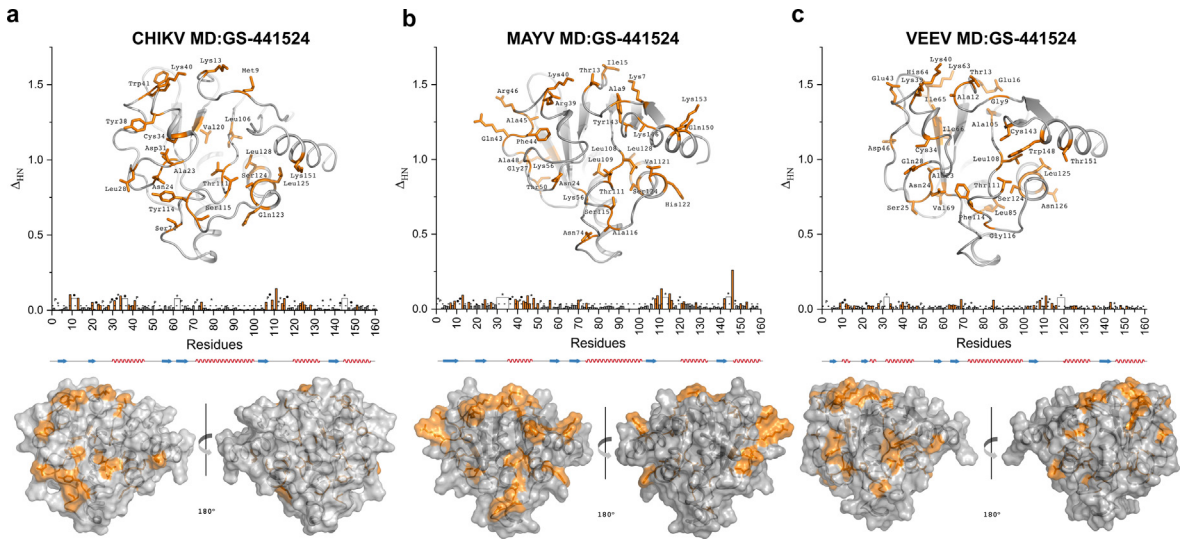

Figure 6. Plot of the combined amide chemical shift changes, $\Delta\delta$, induced by GS-441524 binding versus (a) CHIKV MD, (b) MAYV MD, (c) VEEV MD amino acid sequences at 1:10 molar ratio of protein:ligand. In each plot, the dotted line indicates the applied threshold, an asterisk indicates an unassigned residue of free MD, p indicates a proline residue, and a dot indicates a residue whose HN resonance could not be detected at final titration step. Insets at each plot indicate the mapping of the residues exhibiting meaningful CSPs (value > threshold). Lower panel from each diagram the mapping as in insets on the surface representation. Mapping has been conducted on CHIKV MD, MAYV MD and VEEV MD using the PDB IDs 7P27, 5IQ5 and 5ISN respectively.

assigned only in the free forms. In case of MERS-CoV, the triple glycine motif remained unassigned in both forms (free and ADPr bound). Notably, a different behavior has been observed for *Alphaviruses* MDs for the corresponding loops. In our previous NMR studies, it was reported that these regions in free form of MAYV and CHIKV MDs are characterized by increased mobility on NMR time scale ps-ns.[18,31] Moreover, the backbone assignment of many of these residues was possible only upon ADPr binding indicating that ligand-binding reduces backbone flexibility and impose a compact complex structure. Also, in VEEV MD, this loop undergoes a rearrangement (~3Å) to create a wider pocket.[18]

All the above-mentioned interactions occur on a slow exchange time regime on NMR time scale (~0.1–1 s, $k_{ex} < <|\Delta\nu|$), and this time scale can be associated with dissociation constants K_D values in micromolar or sub-micromolar range[55]. These results are comparable with ITC measurements reported in literature.[52]

The affinity of GS-441524 for all the three CoVs MDs has been determined by protein-detected NMR titrations. SARS-CoV-2 titration analysis highlights a well-defined pocket comparable to the one of the ADPr excluding segments β3-α2,β5-α4, β6-α5. These excluded regions are mainly located in proximity to the phosphate groups and distal ribose and remain unaffected by the binding of GS-441524. The amino acids spanning the β2-α1 and β6-α5 regions are in slow exchange regime, as in the case of ADPr,indicating similar binding affinity. The β3-α2 loop residues which could not be identified upon ADPr binding, exhibit fast exchange between the free and the bound form and only for V253 meaningful CSP value is observed (Figure 4(a)).

On the other hand, titration of SARS-CoV-1 and MERS-CoV MDs with GS-441524 results in remarkably lower CSPs values, compared to those resulting from ADPr titration (Figure 5(a), (b)) and at the limit that an interaction can be interpreted (<0.2).[56] Nonetheless, the mapping revealed in both cases that the meaningful CSPs define a wider interaction region around the ADPr binding site (Figures 4(a), 5(a), 5(b)). Interestingly, the two loops β2-α1 and β6-β5, considered important for the ADPr binding, are characterized by intermediate and fast exchange regime for SARS-CoV-1 and MERS-CoV, respectively. These findings suggest lower affinities compared to ADPr and clearly different affinities amongst the three CoV MDs for GS-441524, agreeing with the observed differences for GS-441524 through the de-MARylation assays.

Further analysis of relaxation parameters (R_1, R_2 and heteronuclear NOE) highlights that those specific regions that involve the D226 and F360 residues in respect to SARS-CoV-2 MD numbering are highly perturbed by the ligands. Indeed, in the case of SARS-CoV-1 MD and MERS-CoV MD the binding of ADPr (Figure S2) induce these amino acids' NHs and their neighboring segments to be broadened beyond

detection similarly to what is observed in the case of SARS-CoV-2 MD[57] even though for MERS-CoV this exchange broadening affects shorter segments. Furthermore, we observed a completely different dynamic behavior for the binding of GS-441524 for SARS-CoV-1 and MERS-CoV MDs (Figure S2). In this case, the binding of GS-441524 induces more rigidity to the above-mentioned regions in SARS-CoV-2 MD (Figure S3) compared to what happens to SARS-CoV-1 and MERS-CoV MDs since in the latter cases signals of D226 and F360 regions are broadened beyond detection indicating different time scale or different exposure to the solvent.

Also, the *Alphaviruses* MDs were titrated with GS-441524 and chemical shift perturbation (CSPs) analysis demonstrates a profile closer to that one of SARS-CoV-1 MD, suggesting a weak interaction. Specifically, segments β1-β2-α1,β4-α2 (β5-α4 on SARS-CoV-2 MD), β5-α3 (β5-α5 on SARS-CoV-2 MD) and residues on α4helix show meaningful CSPs. The interactions are characterized mainly by fast and intermediate exchange regime between bound and free form (Figure 6). These regions are also located around the ADPr binding pocket.

Adenosine, due to its similarity to the GS-441524, was used for comparative studies. The interaction with SARS-CoV-2 MD showed interacting residues in fast exchange regime. Comparing the adenosine structure to the one of GS-441524 we understand that both N positions at the adenine or adenine-like ring and the CN group are important for the different binding affinity (Figure S1).

Isothermal titration calorimetry

In parallel with NMR analysis, we carried out ITC analysis of binding. ITC and NMR data are highly similar, in agreement with previously published results for the studied viral MDs interactions with ADPr.[50,52] Interactions of all tested MDs with ADPr are characterized with significantly higher favorable enthalpy contribution in comparison to that for GS-441524. The second phosphate and the distal ribose groups of ADPr form respectively-three and two intermolecular hydrogen bonds to SARS-CoV-2 MD residues in the segments β3-α2, β5-α4, β6-α5 (6YWL). These hydrogen bonds are the most prominent source of favorable enthalpy for MD: ADPr binding. Accordingly, these two groups are not present in the GS-441524, and therefore, the binding of GS-441524 to MDs is mostly driven by favorable (positive) entropy changes (Table 2). While SARS-CoV-1, SARS-CoV-2 and to some extent MERS-CoV MDs could compensate the lack of the intermolecular hydrogen bonds by some other intermolecular contacts upon GS-441524 binding, the CHIKV and both human MD2 seem are not. Therefore, the K_D values of SARS-CoV-1 and SARS-CoV-2 binding to ADPr and GS-441524 are not significantly different (6.6 and 10.3 μM for SARS-CoV-2, 4.2 μM and 13.6 μM for SARS-CoV-1, respectively), but the K_D values for CHIKV and hPARP14/15 MDs are strongly variated (Figure 7 and Table 2). Note that both binding enthalpy values of interactions between MERS-CoV, CHIKV and hPARP14/15 MDs and GS-441524 allowed estimated K_D values only.

Structural analysis of SARS-CoV-2 MD with GS-441524

The overall comparison of the ADPr bound structure with the GS-441524 resolved in this study (PDB: 7QG7), highlight specific differences at the regions that are close to each small molecule (Figure S4(b), (c)). These are mainly the regions that are involved in the binding of the phosphate groups and the distal ribose of the ADPr, moieties that are missing from the GS-441524 scaffold.

The crystal structure reveals a network of hydrogen bonds involving residues which are among those which have exhibited meaningful chemical shift changes during the NMR titration experiments (Figures 4 and S4). In particular, the adenine-like (pyrrolotriazine) ring of the GS-441524 molecule participates in three hydrogens bonds with the side chain of D226 and the backbone atoms of I227 and F360. Further, 3D $^{13}C/^{15}N$-filtered NOESY of the GS-441524 with uniformly labelled $^{15}N,^{13}C$-labelled SARS-CoV-2 MD was performed on the complex in solution. Indeed, intermolecular NOEs were observed for the bound GS-441524 (Figure 8(a), (b), (c)) and show quite conclusively that the interaction observed for I227 and F360 in the crystal structure is also present in solution as well. The pyrrolotriazine ring exhibit an orientation to the phenylalanine ring similar to the one observed in ADPr bound structure. F360 backbone atoms also form a bond with the CN group, further stabilized via the backbone of D361 (Figure S4(c)).

F360 and its adjacent residues impact SARS-CoV-2 – GS-441524 binding selectivity

Looking at the other viral MDs sequences we observed some interesting differences. The D226-I227 motif is substituted by D-A in MERS-CoV. The F360-D361 is replaced by N-D, N-S, R-D, H-P and F-Q residues in SARS-CoV-1, MERS-CoV, *Alphaviruses* and hPARP14 MD2 and hPARP15 MD2 MDs respectively, (Figure 8(d)). It is possible that the dyad comprised of an aromatic residue (such as phenylalanine) and an adjacent aspartate, is crucial for the conformational adaptation of the protein backbone to the bound small molecule resulting in a stable complex and provides an appropriate orientation to the protein backbone stabilizing the small molecule.

To evaluate the impact of these residues, SARS-CoV-2^{F360N} MD, SARS-CoV-$2^{A358V/F360N}$ MD,

Table 2 Thermodynamic parameters of the interaction between MD-containing proteins and their ligands (ADPr and GS-441524).

	ΔH [kcal/mol]	ΔS [cal/mol K-1]	-T*ΔS [kcal/mol]	ΔG [kcal/mol]	KA [105 M-1]	K_D [μM]	N
			ADPr				
SARS-CoV-2	−8.98 ± 0.21	−6.4	+1.91	−7.07	1.51 ± 0.05	6.6	0.95 ± 0.02
SARS-CoV-2^{F360N}	−9.97 ± 0.08	−10.2	+3.04	−6.93	1.22 ± 0.02	8.2	0.96 ± 0.01
SARS-CoV-1	−11.39 ± 0.08	−13.6	+4.05	−7.34	2.40 ± 0.07	4.2	1.07 ± 0.01
MERS-CoV	−11.24 ± 0.06	−12.7	+3.79	−7.45	2.87 ± 0.07	3.5	0.99 ± 0.01
MERS-CoV^{N410F}	−11.10 ± 0.29	−12.1	+3.61	−7.49	3.02 ± 0.28	3.3	1*
CHIKV	−5.87 ± 0.08	+4.2	−1.26	−7.14	1.70 ± 0.06	5.9	1.00 ± 0.01
hPARP14 MD2	−9.00 ± 0.07	−5.8	+1.73	−7.27	2.13 ± 0.04	4.7	0.96 ± 0.01
hPARP15 MD2	−5.69 ± 0.14	+2.4	−0.70	−6.39	0.49 ± 0.03	20.5	1*
			GS-441524				
SARS-CoV-2	−5.25 ± 0.13	+5.2	−1.55	−6.80	0.97 ± 0.08	10.3	1*
SARS-CoV-2^{F360N}	−4.20 ± 0.04	+7.9	− 2.35	− 6.55	0.63 ± 0.02	15.9	1*
SARS-CoV-1	−2.79 ± 0.08	+12.9	− 3.85	− 6.64	0.74 ± 0.07	13.6	1*
MERS-CoV	−1.09 ± 0.02	+15.8	− 4.71	− 5.80	0.17 ± 0.01	57.5	1*
MERS-CoV^{N410F}	−0.93 ± 0.03	+16.8	−5.01	−5.93	0.23 ± 0.01	43.9	1*
CHIKV	N.D.	-	-	-	N.D.	∼100**	N.D.
hPARP14 MD2	N.D.	-	-	-	N.D.	∼250**	N.D.
hPARP15 MD2	N.D.	-	-	-	N.D.	∼100**	N.D.

* The number of binding sites (N) was fixed to 1.0 upon fitting.
** Estimated values.

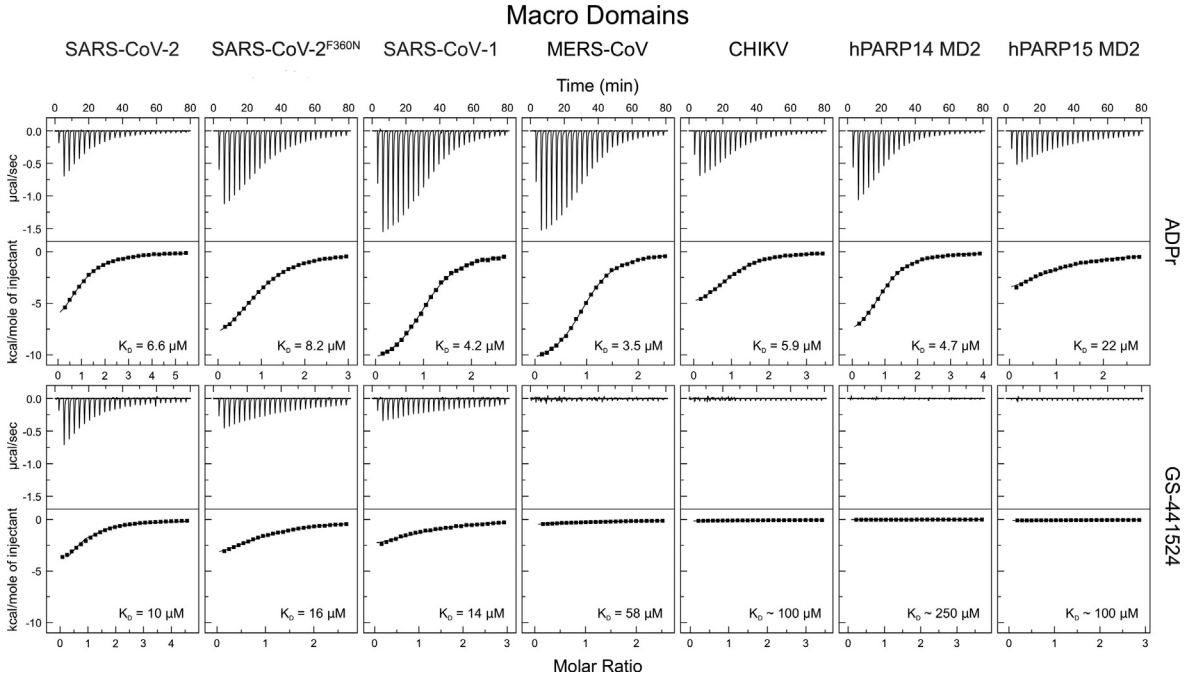

Figure 7. ITC analysis of the interaction between selected MDs and ADPr (upper plots) or GS-441524 (lower plots). The upper graph in each plot shows the raw measurement; the lower graph represents the intergraded heat per injection (squares) and best fit function (solid line). Resulting K_D values are presented for each interaction. All thermodynamic parameters are summarized in Table 2.

SARS-CoV-2$^{F360N/D361S}$ MD and MERS^{N410F} MD mutants were designed and expressed. De-MARylation assays were also performed and the initial substrate decay rate (k) for SARS-CoV-2^{F360N} MD in absence and presence of ADPr and GS-441524 indicates that ADPr affects the mutant's de-MARylation activity in a similar way with that observed for the wild type. On the other hand, GS-441524 seems to affect less the F360N mutant's enzymatic capacity exhibiting a similar effect compared to that observed for the SARS-CoV-1 MD (Figure 2(b)). The double mutants led

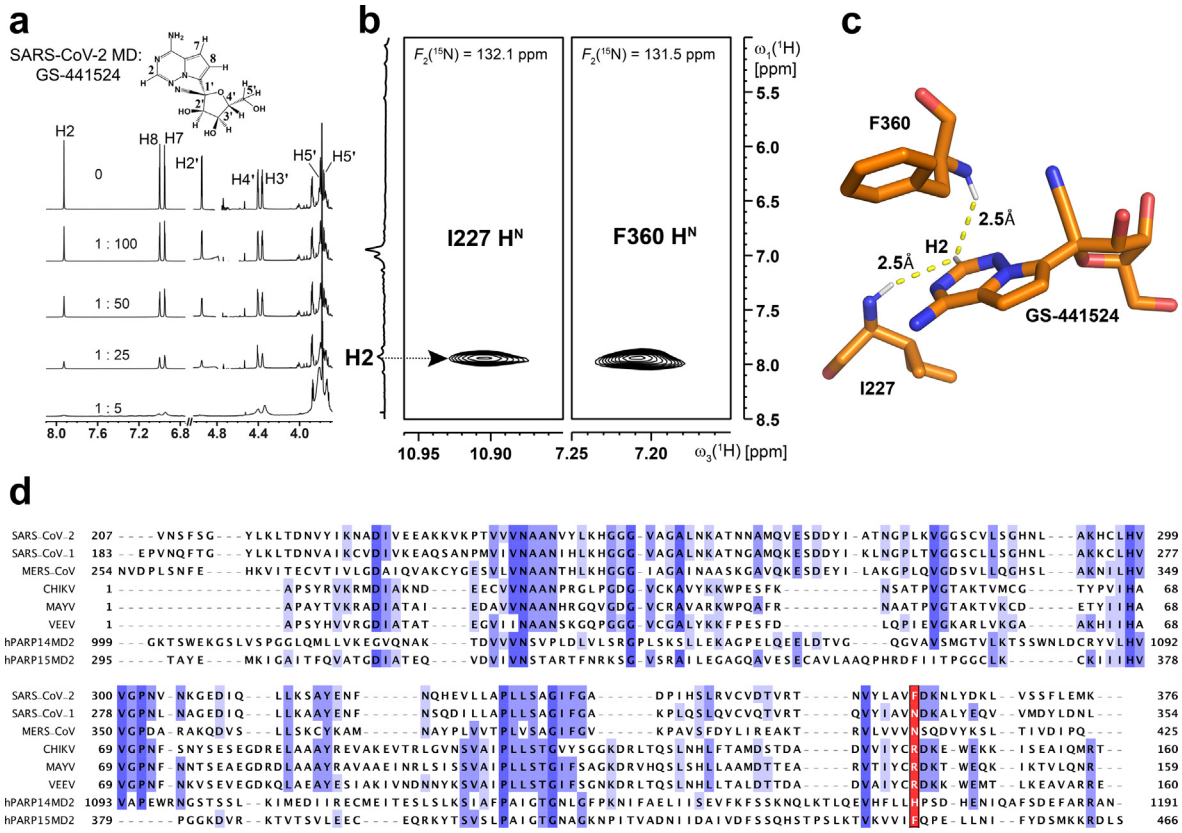

Figure 8. SARS-CoV-2 MD•GS-441524 intermolecular NOEs. (a) Ligand observed ^{1}H (^{13}C/^{15}N-filtered) titration of GS-441524 with SARS-CoV-2 MD. (b) Planes at the amide ^{15}N chemical shifts of I227 and F360 are shown. Intermolecular NOEs are observed between the H2 proton of the GS-441524 and the backbone amide protons of I227 and F360. (c) Backbone amide protons of I227 and F360 are in close proximity to the H2 proton of GS-441524 as observed in the crystal structure of the complex (7QG7). (d) Sequence alignment of the studied herein MDs. Numbering according to nsP3 sequence of each virus and hPARPs full length. In red box is marked the F360 substituted by N at the same position in SARS-CoV-1 and MERS-CoV MDs, R in *Alphaviruses* MD sequences being H and F at hPARP14 MD2 and hPARP15 MD2 respectively.

to further decrease of the inhibitory effect of the GS-441524 without dramatic changes of the ADPr binding capacity of SARS-CoV-2 MD. Specifically, the comparison of the initial substrate decay rates (k) between the free forms and in the presence of ADPr showed 64.7 and 62% decrease while GS-441524 causes 33.2% and 24.9% drop of the k value for SARS-CoV-2$^{A358V/F360N}$ MD and SARS-CoV-2$^{F360N/D361S}$ MD respectively (Figure S5 and S7). MERS-CoV^{N410F} mutant retained a similar initial substrate decay rate behavior to the wild type in the presence of ADPr (69.1% decrease of the k value), while the k value in case of GS-441524 was reduced by 30% compared to the free form (the respective change for the wild type was calculated to 24%) (Figure S5). The results gave an interesting perspective regarding the significance of these residues.

Protein-based titrations with ADPr and GS-441524 were monitored by NMR and CSPs analysis were performed. The interaction of the mutants with the ADPr still occurs in the slow exchange time regime while surprisingly the GS-441524 is characterized by intermediate to fast exchange for the mutant of SARS-CoV-2^{F360N} while the double mutants and MERS-CoV^{N410F} are in a fast exchange regime of the NMR time scale. These findings indicate lower binding affinity compared to the ADPr as well as to the wild-type and GS-441524 interaction. This phenomenon has also been observed for all the other viral MDs studied herein. Although the CSPs values of the SARS-CoV-2^{F360N} mutant are still comparable to the wild type for both molecules (Figure 4(b)), the double mutants caused smaller chemical shift changed (Figure S5).

Notably, the CSP analysis between the SARS-CoV-2^{wt} and the SARS-CoV-2^{F360N} mutant revealed that this substitution affects not only the surrounding residues (the C-terminal segment where F360 is located), but also the residues located at the loop that contains the D226-I227 motif. This is an interesting finding because this loop is actively implicated in the accommodation

of the aromatic ring of adenine and the ring of GS-441524 (Figure S6). This fact together with the differences caused at the de-MARylation activity and the NMR protein-based titrations upon double mutations substitutions, provides an atomic-level insight into the role of amino acid chemical groups to tune the selectivity of MDs against their potential ligands and offer new possibilities in the discovery of new compounds with enhanced inhibitory activity. These findings are further supported by the recently published work of *Correy et al.*.[58] They have reported the critical role of the water molecules present in the cavity and the "bridges" that are created within the loop where these residues are located, in stabilizing the ligand. Moreover, they have provided evidence for the network of hydrogen bonds between N224 sidechain and the backbone of the F360-D361 pair. These residues comprised an amino acid segment in SARS-CoV-2 MD, which is unique among the viral and human MDs studied herein and this may impact the SARS-CoV-2 MD selectivity.

To quantify and compare these findings we also performed ITC measurements for SARS-CoV-2^{F360N} MD mutant and MERS-CoV^{N410F} with ADPr and GS-441524. The binding affinity of SARS-CoV-2^{F360N} MD mutant drops for both ADPr and GS-441524 (K_D values for ADPr and GS-441524 measured 8.2 μM and 15.9 μM, respectively) compared to the wild type (K_D values for ADPr and GS-441524 6.6 μM and 10.0 μM, respectively). According to these findings, it is speculated that this difference in dissociation constants is determined not only by the total buried hydrophobic area, but also by some enthalpy terms, hydrophobic interactions due to π-π stacking.[36] The MERS-CoV^{N410F} MD affinity for ADPr is not affected by the substitution while the K_D value for GS-441524 was decreased to 43.9 μM compared to the 57.5 μM of the wild-type.

All the above led to the conclusion that the sequence pattern at the loop before the α6 (or α4 for *Alphaviruses* MDs) helix, together with the groups that GS-441524 contains, are the elements that alter and tune the selectivity of SARS-CoV-2 entire cavity to the small molecule.

Concluding remarks

In the recent years, ADP-ribosylation is in the spotlight, emerging as a significant process in the regulation of cell biochemistry. Furthermore, several recent studies have reported the importance of this PTM to host defense mechanisms against viral infections. Macro-PARPs are amongst the enzymes that contribute to NAD^+ metabolism by auto and hetero modification, while they can bind ADP-ribosylated substrates to modulate host immune response. A major factor that plays a crucial role in this process, counteracting PARPs activity, is the characteristic property of the viral MDs that can hydrolyze the ADPr moieties from MARylated substrates. This property renders viral MDs the characteristics of potential therapeutic targets. A drawback in the design of highly selective viral MDs binders, is the sequence similarity to the human MD homologs. The in-depth atomic resolution level knowledge of the conformational differences of both viral and human MDs for efficient screening of chemical libraries, are of high importance.

In this study, we investigate whether the nucleotide-based GS-441524, a metabolite of remdesivir, can modify the de-MARylation capacity of MDs derived from CoVs and *Alphaviruses*. De-MARylation based biochemical assay shows that GS-441524 decreases the activity rate of SARS-CoV-2 MD, with no similar effect in the other tested viral MDs. Furthermore, ITC proves that SARS-CoV-2 MD binds tightly GS-441524, based on K_D values. The respective measurements for hPARP14 MD2 and hPARP15 MD2, that are closely related human homologs, showed no interaction with GS-441524.

High-resolution NMR studies in concert with X-ray crystallography, provides atomic-level view on the SARS-CoV-2 complex with GS-441524, suggesting that the F360 and the adjacent residues are crucial determinants for the ligand selectivity and tight binding. The π-π stacking of the aromatic ring with the pyrrolotriazine group of the molecule, observed in the X-rays model, indicate that SARS-CoV-2 MD binding pocket can "capture" efficiently the GS-441524, despite this compound lacks the phosphate groups and distal ribose region that contribute to the strong binding of ADPr compared to adenosine. The formation of a compact structure for the SARS-CoV-2 MD•GS-441524 complex is also manifested by the relaxation data at ps-ns time scale. Additionally, the selectivity is also enhanced by the CN group interaction to the protein backbone while the molecule is hydrogen-bonded by its pyrrolotriazine group to the conserved "D-I" amino acid motif, which seems to act as an anchor, docking the small molecule in the appropriate position. The unique differences between the host and the viral MDs identified in this study should enable the application of better strategies for the design of small molecule inhibitors specific for viral MDs.

Materials and Methods

Constructs design

The CoVs MDs coding sequences used in this study are SARS-CoV-2 residues 207–376 (GenBank entry MN908947.3), SARS-CoV-1 residues 183–354 (GenBank entry NC_004718.3), MERS CoV residues 254–427 (Uniprot entry K9N638) according to nsP3 numbering. SARS-CoV-2 MD gene was cloned into pET28a(+) vector containing an N-terminal His_6-tag and a

tobacco etch virus (TEV) cleavage site. SARS-CoV-2^{F360N} MD mutant has been provided as a synthetic codon optimized sequence gene for expression in *E. coli*, from Twist Biosciences, cloned into pET28a(+) expression vector. The SARS-CoV-$2^{A358V/F360N}$ MD and SARS-CoV-$2^{F360N/D361S}$ MD mutants were created from the later plasmid using site-directed mutagenesis and the used primers sequences are: 5′- GTATA CCTCGTTGTGAATGATAAG −3′ and 5′- CTTAT CATTCACAACGAGGTATAC −3′ for SARS-CoV-$2^{A358V/F360N}$ and 5′- CTCGCCGTGAATAGCA AGAACCTGTAC −3′ and 5′- GTACAGGTT CTTGCTATTCACGGCGAG −3′ for SARS-CoV-$2^{F360N/D361S}$. The sequences of the mutated products were verified by DNA sequencing. The expressed polypeptides contain an N-terminal His_6-tag and a tobacco etch virus (TEV) cleavage site. The studied polypeptides of SARS-CoV-2 MD contain three artificial N-terminal residues. SARS-CoV-1 and MERS-CoV MDs genes have been purchased as codon optimized sequences for expression in *E. coli*, synthetic genes from GenScript, (Piscataway, NJ), cloned into pET20b (+) expression vector. The MERS-CoV^{N410F} MD was created using site-directed mutagenesis using primers sequences: 5′- GTTCTGGTGGTTGT GTTCAGCCAGGACG −3′ and 5′- CGTCCTGGC TGAACACAACCACCAGAAC −3′. The sequence of the mutated product was verified by DNA sequencing. The expressed sequences contain N- and C-terminal uncleavable His_6-tag respectively. SARS-CoV-1 MD contains 7 artificial residues at N-terminus while MERS-CoV MD 10 artificial residues at C-terminal.

The *Alphaviruses* MDs coding sequences are CHIKV residues 1–160 (GenBank entry AJD20049.1) MAYV 1–159 (GenBank MK070492.1) and VEEV 1–161 (GenBank NP_740698) according to nsP3 numbering and have been used their constructs from previously reported studies.[59–61]

The human MDs coding sequences are hPARP14 MD2 residues 999–1191 of the full-length hPARP14 (Uniprot entry Q460N5) and hPARP15 MD2 residues 295–466 of the full-length hPARP15 (Uniprot entry Q460N3). Genes corresponding to hPARP14 MD2 and hPARP15 MD2 were amplified from synthetic, and codon optimized for *E. coli* expression genes, purchased from Twist Biosciences, and cloned into pETM-41 vector. The used primers sequences are: 5′- CAT GCCATGG GAGGTAAGACATC-3′ and 5′- ATAGT TTAGCGG CCGCTTATTAATTTGCGCGA C-3′ for hPARP14 MD2 and 5′- CATGCCATGGGAACTGCTTACGA GATGAAG-3′ and 5′- ATAGTTTAGCGGCCGCTT ATTAACTAAGGTCACGC-3′ for hPAR P15 MD2.

The produced polypeptides contain an N-terminal His_6-MBP-tag and a tobacco etch virus (TEV) cleavage site while the studied contain four artificial N-terminal residues (GAMG).

All the created constructs were verified by DNA sequencing.

The codon optimized cDNA sequence coding the catalytic domain hPARP10 (hPARP10 CD) residues 806–1025 (GenBank entry BC014229.2) was obtained from GenScript, (Piscataway, NJ) into a pGEX-4T-1 vector providing an N-terminal GST-fusion tag.

Protein Expression and Purification

The wild type of viral MDs' expression has been described extensively elsewhere.[57,59–62] For SARS-CoV-2^{F360N}, SARS-CoV-$2^{A358V/F360N}$ and SARS-CoV-$2^{F360N/D361S}$ MD mutants expression E. cloni® EXPRESS BL21(DE3) cells were used, while for the expression of MERS-CoV^{N410F} the Rosetta™ 2(DE3)pLysS cell line. Induction was conducted using 1 mM IPTG and incubation at 18 °C and 180 rpm for 14–16 h. The purification was done as for wild type with minor adjustments. For the expression and purification of hPARP MDs plasmids were transformed in Rosetta™ 2(DE3) pLysS. LB pre-cultures were inoculated and were incubated at 37 °C at 180 rpm for 14–16 h. Then LB cultures were inoculated, and the expression was induced at OD_{600} 0.6–0.8 by 1 mM IPTG at 18 °C for 14–16 h. Cells were harvested and re-suspended with lysis buffer containing. 10 mM imidazole, 50 mM Tris-HCl pH 8, 500 mM NaCl and 25 μL of protease inhibitor cocktail (Sigma Aldrich® P8849) and sonicated. DNase was added and centrifugation at 4 °C and 20.000 rpm (Thermo Scientific®, Sorvall Lynx 6000) for 30 min was performed. The soluble fraction containing the His_6-MBP-tagged MD were loaded onto a HisTrap™ FF affinity column (GE Healthcare) that had been previously equilibrated with 0.1 M $NiSO_4 \cdot 6H_2O$ and binding buffer (10 mM imidazole, 50 mM Tris-HCl pH 8, 500 mM NaCl). The column was washed with a step gradient of imidazole in binding buffer (10, 20, 40, 100, 200, 400 mM). The two human MDs eluted in 20–200 mM imidazole as it was verified by a 15% SDS-PAGE. With the use of an Amicon® Ultra 15 mL Centrifugal Filter membrane (nominal molecular weight cutoff 10 kDa) each protein was concentrated to final volume of 5 mL, and as well buffer exchange was performed, from the elution buffer to 50 mM Tris-HCl pH 8, 300 Mm NaCl and 500 μl of TEV (1 mg/mL) were added and was incubated over night at 4 °C. After 16 h, HisTrap was performed, the MDs eluted in the flow through and 10 mM imidazole fractions and the His_6-MBP-tag at 400 mM. With the use of an Amicon® Ultra 15 mL Centrifugal Filter membrane (nominal molecular weight cutoff 10 kDa) the protein was concentrated to final volume of 1 mL, and as well buffer exchange was performed, from the elution buffer to 50 mM HEPES pH 7, 50 mM NaCl, 2 mM EDTA. As a final step molecular exclusion chromatography was performed using

Superdex 75 Increase 10/300 GE Healthcare column. The fractions that contained the pure protein were pooled together and were concentrated to the desired concentration.

GST-tagged hPARP10 CD was expressed in *E. coli* strain, Rosetta™ 2(DE3)pLysS, in LB. The protein expression was induced at OD 0.7 using 0.7 mM IPTG after 3 h adaptation at 18 °C. The cells were harvested after 15 h incubation at 18 °C, 180 rpm. Cells were resuspended in 50 mM Tris pH 8 containing 300 mM NaCl. Lysozyme 1 mg/ml was added followed by 2 h incubation at 37 °C, 180 rpm. Then, 20% glycerol, 2 mM DTT, 2 mM EDTA and PIC (protease inhibitors cocktail-P8849 Sigma) were added and the cells were sonicated using Amp: 50%, pulse on: 30 sec, pulse off: 30 sec, number of cycles: 7. The cells were centrifuged at 14.000 rpm for 30 min at 4 °C. The supernatant was filtered through a 0.2 μm pore filter and GSTrap affinity chromatography was applied for the isolation. The protein was eluted in GST elution buffer containing 50 mM Tris pH 8, and 10 mM reduced glutathione. hPARP10 CD was buffer exchanged to 50 mM HEPES pH 7.5, 150 mM NaCl, 0.2 mM DTT, 10% glycerol.

Auto-modification of hPARP10 CD

Purified hPARP10 CD was incubated with β-NAD (β-NAD^+, Apollo Scientific), 1:100 molar ratio, for 60 min at 37 °C in 50 mM HEPES pH 7.5, 150 mM NaCl, 0.2 mM DTT, 0.02% IGEPAL® CA-630. The MARylated hPARP10 CD was further purified by size exclusion chromatography (SEC) using Superdex Increase 200 10/300 GL in 50 mM HEPES pH 7.5, 150 mM NaCl, 0.2 mM DTT. The obtained fractions were pooled together supplemented with 10% glycerol, aliquoted and stored at −80 °C.

hPARP10 CD de-MARylation assay

1 μM of MARylated hPARP10 CD was added to reaction tube containing 1 μM MD in absence or presence of the mentioned ratios of ADPr, GS-441524 and remdesivir in 50 mM HEPES pH 7.5, 150 mM NaCl, 0.2 mM DTT, 0.02% IGEPAL® CA-630 and 2% DMSO. All the reactions were incubated at 30 °C at 250 rpm for the indicated time. Reactions were stopped by adding 3x FSB containing 150 mM DTT. The samples were heated for 5 min at 92 °C, centrifuged for 5 min at 14.000 rpm and 4 °C and separated in 12% acrylamide SDS-PAGE. Independent experiments n = 3 or n = 2.

Immunoblotting

The separated proteins were transferred to Polyvinylidene fluoride (PVDF) 0.45 μM pore size membrane (Immobilon P-Merck Millipore) using Trans-Blot® Turbo™ Transfer System (BioRad). The blot was blocked by 5% non-fat dry milk in Tris-Buffered Saline (TBS) pH 7.5 buffer, containing 0.1% Tween 20 for 1 h at RT followed by 14–16 h incubation at 4 °C with anti-mono ADPr reagent MABE1076 (Sigma). As secondary antibody for the detection, anti-rabbit IgG HRP-linked (7074-Cell Signaling Technology) was used. For the visualization a ChemiDoc Imaging System (BioRad) was used, and Image Lab software used for the quantification.

Quantification of the initial rate of substrate decay (k)

The calculation of the initial rate of substrate decay was based on the literature.[52] The quantification results for each reaction were plotted versus time, and exponentially fitted following the functional form: $([S]initial-[S]final)e^{-[k/([S]initial)t]} + [S]final$ for parameter k calculation, using Origin2019b.

NMR titrations/binding studies of ADPr and GS-441524

Interaction studies were performed using NMR spectroscopy. For NMR measurements the used buffer for wild type SARS-CoV-2 MD was 25 mM Bis–Tris pH 6.5, 150 mM NaCl, 3 mM tris-(2-carboxyethyl)-phosphine (TCEP) while for all the other MDs 10 mM HEPES pH 7, 20 mM NaCl, 2 mM DTT, 2 mM EDTA. NMR samples also contained 10% D_2O and 0.25 mM DSS (4,4-Dimethyl-4-silapentane-1-sulfonic acid 4,4-Dimethyl-4-silapentane-1-sulfonic acid). NMR titrations were performed on sample with incremental [protein]:[small molecule] ratios (e.g. 1:0.25, 1:0.5, 1:1, 1:3, 1:10). ^1H, ^{15}N HSQC spectrum was recorded after each addition. The titrations were concluded at 1:10 ratio. Combined amide chemical shift perturbations were calculated using the equation: $\Delta\delta = [(\Delta\delta_{HN})^2 + (\Delta\delta_N/5)^2]^{1/2}$[56] and backbone assignment of the free or/and the bound forms of the proteins have been previously reported (BMRB codes 50387, 50388, 50993, 50969, 50970, 50971, 27158, 30043, 25132). The meaningful chemical shift perturbations were derived calculating a threshold value for each of the studied interactions. The threshold was set using the standard deviation (σ) iteratively calculated. Residues exhibiting chemical shift perturbation value greater than 3σwere excluded at each time. The threshold value at the end resulted in considering meaningful residues that have a value higher of the sum of the average plus a standard deviation.

^{15}N-relaxation studies

^{15}N labelled samples for dynamics studies by NMR spectroscopy were prepared in the same buffers used for their NMR assignments experiments. Relaxation experiments (^{15}N T_1, T_2 and $\{^1H\}$–^{15}N NOE) on all the CoV MDs in the free

and bound forms [SARS–CoV–2 MD (only on the GS-441524 bound form), SARS–CoV–1 MD and MERS–CoV MD] were conducted using the Bruker Avance III High-Definition 700 MHz NMR spectrometer equipped with a cryogenically cooled 5 mm four-channel $^{1}H/^{13}C/^{15}N/^{2}H$ Z-gradient probe (TCI) at 298 K. All spectra were processed with TopSpin 4.0.1 and analyzed in CARA software. ^{15}N longitudinal (R_1), transverse (R_2) relaxation and $\{^{1}H\}$–^{15}N heteronuclear NOE data were fitted using Origin software using decay rate analysis tool and error analysis implemented in the software. The delays used for the T_1 were 20, 60, 100, 200, 400, 600, 800, and 1200 ms, and for T_2 were 15.68, 31.36, 62.72, 94.08, 125.44, 156.8, 188.16, and 219.52 ms. The $\{^{1}H\}$–^{15}N heteronuclear NOEs were obtained for ^{1}H–saturated and unsaturated spectra (3 s saturation time).

Isothermal Titration Calorimetry

The ITC experiments were performed at 25 °C using a MicroCal VP-ITC microcalorimeter (Malvern Instruments ltd., UK). All components were equilibrated in the ITC buffer containing 50 mM HEPES pH 7, 50 mM NaCl, 2 mM EDTA. ADPr and GS-441524 at concentrations of 0.45 mM were titrated into 23–35 μM MDs proteins in 26 steps. The ITC-data was analyzed with the ITC-Origin 7.0 software using a “one-site” binding model. The proteins concentrations were calculated from the UV-absorption at 280 nm by Nanodrop spectrophotometer (Thermo Fisher Scientific, DE, USA).

Crystallization, data collection, data processing and refinement

Crystals of SARS-CoV-2 MD in complex with GS-441524 were grown the following way: SARS-CoV-2 MD (18 mg/mL in 20 mM Tris pH 8.0, 150 mM NaCl, 1 mM TCEP) was mixed with a 50 mM stock solution of GS-441524 in 100% DMSO to yield a ligand concentration of 2 mM in the crystallization sample. Crystallization was performed as a vapor diffusion sitting drop experiment in 3552 Corning 96 well protein crystallization plates, using 50 μL of reservoir containing 0.1 M Bis-Tris Propane/HCl pH 7.0, 2.2 M DL-Malic Acid pH 7.0. Drops were set by mixing 0.4 μL of protein-GS-441524 with 0.4 μL of reservoir solution. Plates were incubated at 289.15 K. Crystals were cryoprotected using reservoir supplied with 20% EG.

Diffraction data were collected on beamline 14.2[63] of the BESSY II storage ring, Berlin, Germany at 100 K using a monochromatic X-ray beam (λ = 0.9184 Å) and a PILATUS3 2 M detector. The data were processed using XDSAPP[64]. The structure was solved by molecular replacement with Phaser[65] using the input structure with PDB entry 6YWM[50] as a search model. The structure was further refined using the fspipeline auto-refinement script[66] and subsequently by further iterative cycles of manual model building in Coot[67] and automated refinement using phenix.refine.[68] Geometrical restrains for the GS-441524 ligand were generated using GRADE (GlobalPhasing). Relevant statistics for data processing and refinement are listed in Table S1. The structure and associated structure-factor amplitudes have been deposited in the PDB as entry 7QG7.

3D X-filtered NOESY

Ligand/Protein samples were prepared in buffer containing 25 mM Bis-Tris pH 6.5, 150 mM NaCl, 5% D_2O, 0.15 mM DSS, 0.02% NaN_3, 3.5% DMSO-D_6. All NMR samples had a final volume of 400 μL in a Bruker shaped tube. For the assignment of resonances of GS-441524 bound to ^{15}N,^{13}C-labelled SARS-CoV-2 MD, doubly isotope-filtered 1D ^{1}H excitation sculpting titration experiments were performed with filter delays adjusted to $^{1}J_{NH}$ = 94 Hz, $^{1}J_{CHali}$ = 130 Hz and $^{1}J_{CHaro}$ = 170 Hz. Titration points at stoichiometric ratios of 0, 1:100, 1:50, 1:25 and 1:5 for SARS-CoV-2 MD and GS-441524, respectively, were acquired. The final titration point had a ligand and protein concentrations of 1 mM and 0.2 mM, respectively. 3D F_1-$^{13}C/^{15}N$-filtered NOESY-[^{15}N,^{1}H]-SOFAST-HMQC (τ_m = 150 ms) of the GS-441524 with uniformly labelled ^{15}N,^{13}C-labelled SARS-CoV-2 MD were performed on the 5:1 complex in solution. NMR experiments were carried out at a sample temperature of 298 K on a Bruker Avance III 950 MHz spectrometer equipped with a $^{1}H\{^{13}C/^{15}N\}$ TCI cryoprobe.[69–72]

Accession numbers

PDB: 7QG7.

CRediT authorship contribution statement

Aikaterini C. Tsika: Conceptualization, Investigation, Supervision, Methodology. **Angelo Gallo:** Investigation, Methodology. **Nikolaos K. Fourkiotis:** Investigation, Methodology. **Aikaterini I. Argyriou:** Investigation, Methodology. **Sridhar Sreeramulu:** Conceptualization, Investigation, Supervision. **Frank Löhr:** Investigation, Methodology. **Vladimir V. Rogov:** Investigation, Methodology. **Christian Richter:** Investigation, Methodology. **Verena Linhard:** Investigation, Methodology. **Santosh L. Gande:** Investigation, Methodology. **Nadide Altincekic:** . **Robin Krishnathas:** Investigation, Methodology. **Isam Elamri:** Investigation, Methodology. **Harald Schwalbe:** Conceptualization, Investigation,

Supervision, Funding acquisition, Project administration, Resources. **Jan Wollenhaupt:** . **Manfred S. Weiss:** Funding acquisition, Project administration, Resources. **Georgios A. Spyroulias:** Conceptualization, Investigation, Supervision, Funding acquisition, Project administration, Resources.

DECLARATION OF COMPETING INTEREST

The authors declare that they have no known competing financial interests or personal relationships that could have appeared to influence the work reported in this paper.

Acknowledgement

This work was supported by the INSPIRED (MIS 5002550; ACT, AG, NKF, AIA, GAS) which is implemented under the Action 'Reinforcement of the Research and Innovation Infrastructure,' funded by the Operational Program 'Competitiveness, Entrepreneurship and Innovation' (NSRF 2014–2020) and co-financed by Greece and the European Union (European Regional Development Fund). EU FP7 REGPOT CT-2011- 285950 "SEE-DRUG" project is acknowledged for the purchase of UPAT's 700 MHz NMR equipment.

The work has been conducted also as in-part within the international consortium of Covid19-NMR (covid19-nmr.de). Work at BMRZ is supported by the state of Hesse. Work in Covid19-nmr was supported by the Goethe Corona Funds, by the IWB-EFRE-program 20007375 of state of Hesse, the DFG through CRC902: "Molecular Principles of RNA-based regulation." and through infrastructure funds (project numbers: 277478796, 277479031, 392682309, 452632086, 70653611) and by European Union's Horizon 2020 research and innovation program iNEXT-discovery under grant agreement No 871037.

V.V.R. received funding from Structural Genomic Consortium. V.V.R. received funding from Structural Genomic Consortium. The Structural Genomics Consortium is a registered charity (no: 1097737) that receives funds from Bayer AG, Boehringer Ingelheim, Bristol Myers Squibb, Genentech, Genome Canada through Ontario Genomics Institute [OGI-196], EU/EFPIA/OICR/McGill/KTH/Diamond Innovative Medicines Initiative 2 Joint Undertaking [EUbOPEN grant 875510], Janssen, Merck KGaA (aka EMD in Canada and US), Pfizer and Takeda.

Appendix A. Supplementary Data

Supplementary data to this article can be found online at https://doi.org/10.1016/j.jmb.2022.167720.

Received 23 December 2021;
Accepted 6 July 2022;
Available online 15 July 2022

Keywords:
Remdesivir;
ADP-ribosylation;
PARPs;
Coronaviruses;
Alphaviruses;
Macro domain

Abbreviations:
SARS-CoV-2, Severe Acute Respiratory Syndrome Coronavirus 2; SARS-CoV-1, Severe Acute Respiratory Syndrome Coronavirus; MERS-CoV, Middle East Respiratory Syndrome Coronavirus; CHIKV, Chikungunya virus; MAYV, Mayaro virus; VEEV, Venezuelan Equine Encephalitis virus; ADPr, ADP-ribose; ART, ADP-ribosyl transferase; PARP, poly (ADP-ribose) polymerases; CoV, Coronavirus; MD, Macro domain; NAD, Nicotinamide adenine dinucleotide

References

1. Palazzo, L., Mikolčević, P., Mikoč, A., Ahel, I., (2019). ADP-ribosylation signalling and human disease. *Open Biol.* **9**, 190041.
2. Hoch, N.C., Polo, L.M., (2019). ADP-ribosylation: from molecular mechanisms to human disease. *Genet. Mol. Biol.* **43**, e20190075.
3. Aravind, L., Zhang, D., de Souza, R.F., Anand, S., Iyer, L. M., (2015). The natural history of ADP-ribosyltransferases and the ADP-ribosylation system. *Curr. Top. Microbiol. Immunol.* **384**, 3–32.
4. Gupte, R., Liu, Z., Kraus, W.L., (2017). PARPs and ADP-ribosylation: recent advances linking molecular functions to biological outcomes. *Genes Dev.* **31**, 101–126.
5. Bartlett, E., Bonfiglio, J.J., Prokhorova, E., Colby, T., Zobel, F., Ahel, I., et al., (2018). Interplay of Histone Marks with Serine ADP-Ribosylation. *Cell Rep.* **24** 3488-502.e5.
6. Pellegrino, S., Altmeyer, M., (2016). Interplay between Ubiquitin, SUMO, and Poly(ADP-Ribose) in the Cellular Response to Genotoxic Stress. *Front. Genet.* **7**, 63.
7. Chatrin, C., Gabrielsen, M., Buetow, L., Nakasone, M.A., Ahmed, S.F., Sumpton, D., et al., (2020). Structural insights into ADP-ribosylation of ubiquitin by Deltex family E3 ubiquitin ligases. *Sci. Adv.* **6**
8. Luscher, B., Butepage, M., Eckei, L., Krieg, S., Verheugd, P., Shilton, B.H., (2018). ADP-Ribosylation, a Multifaceted Posttranslational Modification Involved in the Control of Cell Physiology in Health and Disease. *Chem. Rev.* **118**, 1092–1136.
9. Palazzo, L., Mikoč, A., Ahel, I., (2017). ADP-ribosylation: new facets of an ancient modification. *FEBS J.* **284**, 2932–2946.

10. Weixler, L., Schäringer, K., Momoh, J., Lüscher, B., Feijs, K.L.H., Žaja, R., (2021). ADP-ribosylation of RNA and DNA: from in vitro characterization to in vivo function. *Nucleic Acids Res.* **49**, 3634–3650.
11. Koch-Nolte, F., Kernstock, S., Mueller-Dieckmann, C., Weiss, M.S., Haag, F., (2008). Mammalian ADP-ribosyltransferases and ADP-ribosylhydrolases. *Front Biosci.* **13**, 6716–6729.
12. Hottiger, M.O., Hassa, P.O., Lüscher, B., Schüler, H., Koch-Nolte, F., (2010). Toward a unified nomenclature for mammalian ADP-ribosyltransferases. *Trends Biochem. Sci.* **35**, 208–219.
13. Cohen, M.S., Chang, P., (2018). Insights into the biogenesis, function, and regulation of ADP-ribosylation. *Nat. Chem. Biol.* **14**, 236–243.
14. Rack, J.G., Perina, D., Ahel, I., (2016). Macrodomains: Structure, Function, Evolution, and Catalytic Activities. *Annu. Rev. Biochem.* **85**, 431–454.
15. Fehr, A.R., Jankevicius, G., Ahel, I., Perlman, S., (2018). Viral Macrodomains: Unique Mediators of Viral Replication and Pathogenesis. *Trends Microbiol.* **26**, 598–610.
16. Han, W., Li, X., Fu, X., (2011). The macro domain protein family: structure, functions, and their potential therapeutic implications. *Mutat. Res.* **727**, 86–103.
17. Neuvonen, M., Ahola, T., (2009). Differential activities of cellular and viral macro domain proteins in binding of ADP-ribose metabolites. *J. Mol. Biol.* **385**, 212–225.
18. Makrynitsa, G.I., Ntonti, D., Marousis, K.D., Birkou, M., Matsoukas, M.T., Asami, S., et al., (2019). Conformational plasticity of the VEEV macro domain is important for binding of ADP-ribose. *J. Struct. Biol.* **206**, 119–127.
19. Zapata-Pérez, R., Gil-Ortiz, F., Martínez-Moñino, A.B., García-Saura, A.G., Juanhuix, J., Sánchez-Ferrer, Á., (2017). Structural and functional analysis of Oceanobacillus iheyensis macrodomain reveals a network of waters involved in substrate binding and catalysis. *Open Biol.* **7**
20. Atasheva, S., Frolova, E.I., Frolov, I., (2014). Interferon-stimulated poly(ADP-Ribose) polymerases are potent inhibitors of cellular translation and virus replication. *J. Virol.* **88**, 2116–2130.
21. Verheugd, P., Forst, A.H., Milke, L., Herzog, N., Feijs, K.L., Kremmer, E., et al., (2013). Regulation of NF-κB signalling by the mono-ADP-ribosyltransferase ARTD10. *Nat. Commun.* **4**, 1683.
22. Fehr, A.R., Singh, S.A., Kerr, C.M., Mukai, S., Higashi, H., Aikawa, M., (2020). The impact of PARPs and ADP-ribosylation on inflammation and host-pathogen interactions. *Genes Dev.* **34**, 341–359.
23. Iwata, H., Goettsch, C., Sharma, A., Ricchiuto, P., Goh, W. W., Halu, A., et al., (2016). PARP9 and PARP14 cross-regulate macrophage activation via STAT1 ADP-ribosylation. *Nat. Commun.* **7**, 12849.
24. Daugherty, M.D., Young, J.M., Kerns, J.A., Malik, H.S., (2014). Rapid evolution of PARP genes suggests a broad role for ADP-ribosylation in host-virus conflicts. *PLoS Genet.* **10**, e1004403.
25. Strauss, J.H., Strauss, E.G., (1994). The alphaviruses: gene expression, replication, and evolution. *Microbiol. Rev.* **58**, 491–562.
26. Chen, Y., Liu, Q., Guo, D., (2020). Emerging coronaviruses: Genome structure, replication, and pathogenesis. *J. Med. Virol.* **92**, 418–423.
27. Kenney, S.P., Meng, X.J., (2019). Hepatitis E Virus Genome Structure and Replication Strategy. *Cold Spring Harb. Perspect. Med.* **9**
28. Egloff, M.P., Malet, H., Putics, A., Heinonen, M., Dutartre, H., Frangeul, A., et al., (2006). Structural and functional basis for ADP-ribose and poly(ADP-ribose) binding by viral macro domains. *J. Virol.* **80**, 8493–8502.
29. Cho, C.C., Lin, M.H., Chuang, C.Y., Hsu, C.H., (2016). Macro Domain from Middle East Respiratory Syndrome Coronavirus (MERS-CoV) Is an Efficient ADP-ribose Binding Module: CRYSTAL STRUCTURE AND BIOCHEMICAL STUDIES. *J. Biol. Chem.* **291**, 4894–4902.
30. Lin, M.H., Chang, S.C., Chiu, Y.C., Jiang, B.C., Wu, T.H., Hsu, C.H., (2020). Structural, Biophysical, and Biochemical Elucidation of the SARS-CoV-2 Nonstructural Protein 3 Macro Domain. *ACS Infect. Dis.* **6**, 2970–2978.
31. Tsika, A.C., Melekis, E., Tsatsouli, S.A., Papageorgiou, N., Maté, M.J., Canard, B., et al., (2019). Deciphering the Nucleotide and RNA Binding Selectivity of the Mayaro Virus Macro Domain. *J. Mol. Biol.* **431**, 2283–2297.
32. Li, C., Debing, Y., Jankevicius, G., Neyts, J., Ahel, I., Coutard, B., et al., (2016). Viral Macro Domains Reverse Protein ADP-Ribosylation. *J. Virol.* **90**, 8478–8486.
33. Eckei, L., Krieg, S., Bütepage, M., Lehmann, A., Gross, A., Lippok, B., et al., (2017). The conserved macrodomains of the non-structural proteins of Chikungunya virus and other pathogenic positive strand RNA viruses function as mono-ADP-ribosylhydrolases. *Sci. Rep.* **7**, 41746.
34. Leung, A.K.L., McPherson, R.L., Griffin, D.E., (2018). Macrodomain ADP-ribosylhydrolase and the pathogenesis of infectious diseases. *PLoS Pathog.* **14**, e1006864.
35. Alhammad, Y.M.O., Fehr, A.R., (2020). The Viral Macrodomain Counters Host Antiviral ADP-Ribosylation. *Viruses.* **12**
36. Rack, J.G.M., Zorzini, V., Zhu, Z., Schuller, M., Ahel, D., Ahel, I., (2020). Viral macrodomains: a structural and evolutionary assessment of the pharmacological potential. *Open Biol.* **10**, 200237.
37. Russo, L.C., Tomasin, R., Araújo Matos, I., Manucci, A.C., Sowa, S.T., Dale, K., et al., (2021). The SARS-CoV-2 Nsp3 macrodomain reverses PARP9/DTX3L-dependent ADP-ribosylation induced by interferon signalling. *bioRxiv.* 2021.04.06.438552.
38. Lei, J., Kusov, Y., Hilgenfeld, R., (2018). Nsp3 of coronaviruses: Structures and functions of a large multi-domain protein. *Antiviral Res.* **149**, 58–74.
39. Fehr, A.R., Athmer, J., Channappanavar, R., Phillips, J.M., Meyerholz, D.K., Perlman, S., (2015). The nsp3 macrodomain promotes virulence in mice with coronavirus-induced encephalitis. *J. Virol.* **89**, 1523–1536.
40. Fehr, A.R., Channappanavar, R., Jankevicius, G., Fett, C., Zhao, J., Athmer, J., et al., (2016). The Conserved Coronavirus Macrodomain Promotes Virulence and Suppresses the Innate Immune Response during Severe Acute Respiratory Syndrome Coronavirus Infection. *mBio.* **7**
41. Kuri, T., Eriksson, K.K., Putics, A., Züst, R., Snijder, E.J., Davidson, A.D., et al., (2011). The ADP-ribose-1''-monophosphatase domains of severe acute respiratory syndrome coronavirus and human coronavirus 229E mediate resistance to antiviral interferon responses. *J. Gen. Virol.* **92**, 1899–1905.

42. Altincekic, N., Korn, S.M., Qureshi, N.S., Dujardin, M., Ninot-Pedrosa, M., Abele, R., et al., (2021). Large-Scale Recombinant Production of the SARS-CoV-2 Proteome for High-Throughput and Structural Biology Applications. *Front Mol Biosci.* **8**, 653148.
43. Rezagholizadeh, A., Khiali, S., Sarbakhsh, P., Entezari-Maleki, T., (2021). Remdesivir for treatment of COVID-19; an updated systematic review and meta-analysis. *Eur. J. Pharmacol.* **897**, 173926.
44. Kalil, A.C., Patterson, T.F., Mehta, A.K., Tomashek, K.M., Wolfe, C.R., Ghazaryan, V., et al., (2021). Baricitinib plus Remdesivir for Hospitalized Adults with Covid-19. *N. Engl. J. Med.* **384**, 795–807.
45. Saha, A., Sharma, A.R., Bhattacharya, M., Sharma, G., Lee, S.S., Chakraborty, C., (2020). Probable Molecular Mechanism of Remdesivir for the Treatment of COVID-19: Need to Know More. *Arch. Med. Res.* **51**, 585–586.
46. Tempestilli, M., Caputi, P., Avataneo, V., Notari, S., Forini, O., Scorzolini, L., et al., (2020). Pharmacokinetics of remdesivir and GS-441524 in two critically ill patients who recovered from COVID-19. *J. Antimicrob. Chemother.* **75**, 2977–2980.
47. Yan, V.C., Muller, F.L., (2020). Advantages of the Parent Nucleoside GS-441524 over Remdesivir for Covid-19 Treatment. *ACS Med. Chem. Lett.* **11**, 1361–1366.
48. Kokic, G., Hillen, H.S., Tegunov, D., Dienemann, C., Seitz, F., Schmitzova, J., et al., (2021). Mechanism of SARS-CoV-2 polymerase stalling by remdesivir. *Nat. Commun.* **12**, 279.
49. Li, Y., Cao, L., Li, G., Cong, F., Li, Y., Sun, J., et al., (2021). Remdesivir Metabolite GS-441524 Effectively Inhibits SARS-CoV-2 Infection in Mouse Models. *J. Med. Chem.*.
50. Ni, X., Schröder, M., Olieric, V., Sharpe, M.E., Hernandez-Olmos, V., Proschak, E., et al., (2021). Structural Insights into Plasticity and Discovery of Remdesivir Metabolite GS-441524 Binding in SARS-CoV-2 Macrodomain. *ACS Med. Chem. Lett.* **12**, 603–609.
51. Murphy, B.G., Perron, M., Murakami, E., Bauer, K., Park, Y., Eckstrand, C., et al., (2018). The nucleoside analog GS-441524 strongly inhibits feline infectious peritonitis (FIP) virus in tissue culture and experimental cat infection studies. *Vet. Microbiol.* **219**, 226–233.
52. Alhammad, Y.M.O., Kashipathy, M.M., Roy, A., Gagné, J. P., McDonald, P., Gao, P., et al., (2021). The SARS-CoV-2 Conserved Macrodomain Is a Mono-ADP-Ribosylhydrolase. *J. Virol.* **95**
53. Lin, M.H., Cho, C.C., Chiu, Y.C., Chien, C.Y., Huang, Y.P., Chang, C.F., et al., (2021). Elucidating the tunability of binding behavior for the MERS-CoV macro domain with NAD metabolites. *Commun Biol.* **4**, 123.
54. Malet, H., Coutard, B., Jamal, S., Dutartre, H., Papageorgiou, N., Neuvonen, M., et al., (2009). The crystal structures of Chikungunya and Venezuelan equine encephalitis virus nsP3 macro domains define a conserved adenosine binding pocket. *J. Virol.* **83**, 6534–6545.
55. Ziarek, J.J., Peterson, F.C., Lytle, B.L., Volkman, B.F., (2011). Binding site identification and structure determination of protein-ligand complexes by NMR a semiautomated approach. *Methods Enzymol.* **493**, 241–275.
56. Williamson, M.P., (2013). Using chemical shift perturbation to characterise ligand binding. *Prog. Nucl. Magn. Reson. Spectrosc.* **73**, 1–16.
57. Cantini, F., Banci, L., Altincekic, N., Bains, J.K., Dhamotharan, K., Fuks, C., et al., (2020). (1)H, (13)C, and (15)N backbone chemical shift assignments of the apo and the ADP-ribose bound forms of the macrodomain of SARS-CoV-2 non-structural protein 3b. *Biomol NMR Assign.* **14**, 339–346.
58. Correy, G.J., Kneller, D.W., Phillips, G., Pant, S., Russi, S., Cohen, A.E., et al., (2022). The mechanisms of catalysis and ligand binding for the SARS-CoV-2 NSP3 macrodomain from neutron and X-ray diffraction at room temperature. *bioRxiv*..
59. Melekis, E., Tsika, A.C., Lichière, J., Chasapis, C.T., Margiolaki, I., Papageorgiou, N., et al., (2015). NMR study of non-structural proteins–part I: (1)H, (13)C, (15)N backbone and side-chain resonance assignment of macro domain from Mayaro virus (MAYV). *Biomol NMR Assign.* **9**, 191–195.
60. Lykouras, M.V., Tsika, A.C., Lichière, J., Papageorgiou, N., Coutard, B., Bentrop, D., et al., (2018). NMR study of non-structural proteins-part III: (1)H, (13)C, (15)N backbone and side-chain resonance assignment of macro domain from Chikungunya virus (CHIKV). *Biomol NMR Assign.* **12**, 31–35.
61. Makrynitsa, G.I., Ntonti, D., Marousis, K.D., Tsika, A.C., Lichière, J., Papageorgiou, N., et al., (2015). NMR study of non-structural proteins–part II: (1)H, (13)C, (15)N backbone and side-chain resonance assignment of macro domain from Venezuelan equine encephalitis virus (VEEV). *Biomol .NMR Assign.* **9**, 247–251.
62. Tsika, A.C., Fourkiotis, N.K., Charalampous, P., Gallo, A., Spyroulias, G.A., (2021). NMR study of macro domains (MDs) from betacoronavirus: backbone resonance assignments of SARS-CoV and MERS-CoV MDs in the free and the ADPr-bound state. *Biomol. NMR Assign.* **1–8**
63. Mueller, U., Förster, R., Hellmig, M., Huschmann, F.U., Kastner, A., Malecki, P., et al., (2015). The macromolecular crystallography beamlines at BESSY II of the Helmholtz-Zentrum Berlin: Current status and perspectives. *Eur. Phys. J. Plus.* **130**, 141.
64. Sparta, K.M., Krug, M., Heinemann, U., Mueller, U., Weiss, M.S., (2016). XDSAPP2.0. *J. Appl. Crystallogr.* **49**, 1085–1092.
65. McCoy, A.J., (2007). Solving structures of protein complexes by molecular replacement with Phaser. *Acta Crystallogr. D Biol. Crystallogr.* **63**, 32–41.
66. Schiebel, J., Krimmer Stefan, G., Röwer, K., Knörlein, A., Wang, X., Park, A.Y., et al., (2016). High-Throughput Crystallography: Reliable and Efficient Identification of Fragment Hits. *Structure.* **24**, 1398–1409.
67. Emsley, P., Lohkamp, B., Scott, W.G., Cowtan, K., (2010). Features and development of Coot. *Acta Crystallogr. D Biol. Crystallogr.* **66**, 486–501.
68. Afonine, P.V., Grosse-Kunstleve, R.W., Echols, N., Headd, J.J., Moriarty, N.W., Mustyakimov, M., et al., (2012). Towards automated crystallographic structure refinement with phenix.refine. *Acta Crystallogr. D Biol. Crystallogr.* **68**, 352–367.
69. Breeze, A.L., (2000). Isotope-filtered NMR methods for the study of biomolecular structure and interactions. *Prog. Nucl. Magn. Reson. Spectrosc.* **36**, 323–372.
70. Zwahlen, C., Legault, P., Vincent, S.J., Greenblatt, J., Konrat, R., Kay, L.E., (1997). Methods for measurement of intermolecular NOEs by multinuclear NMR spectroscopy:

application to a bacteriophage λ N-peptide/boxB RNA complex. *J. Am. Chem. Soc.* **119**, 6711–6721.

71. Ogura, K., Terasawa, H., Inagaki, F., (1996). An improved double-tuned and isotope-filtered pulse scheme based on a pulsed field gradient and a wide-band inversion shaped pulse. *J. Biomol. NMR* **8**, 492–498.

72. Iwahara, J., Wojciak, J.M., Clubb, R.T., (2001). Improved NMR spectra of a protein-DNA complex through rational mutagenesis and the application of a sensitivity optimized isotope-filtered NOESY experiment. *J. Biomol. NMR* **19**, 231–241.